

# Copper-coordinated cellulose ion conductors for solid-state batteries

<https://doi.org/10.1038/s41586-021-03885-6>

Received: 23 November 2020

Accepted: 6 August 2021

Published online: 20 October 2021

 Check for updates

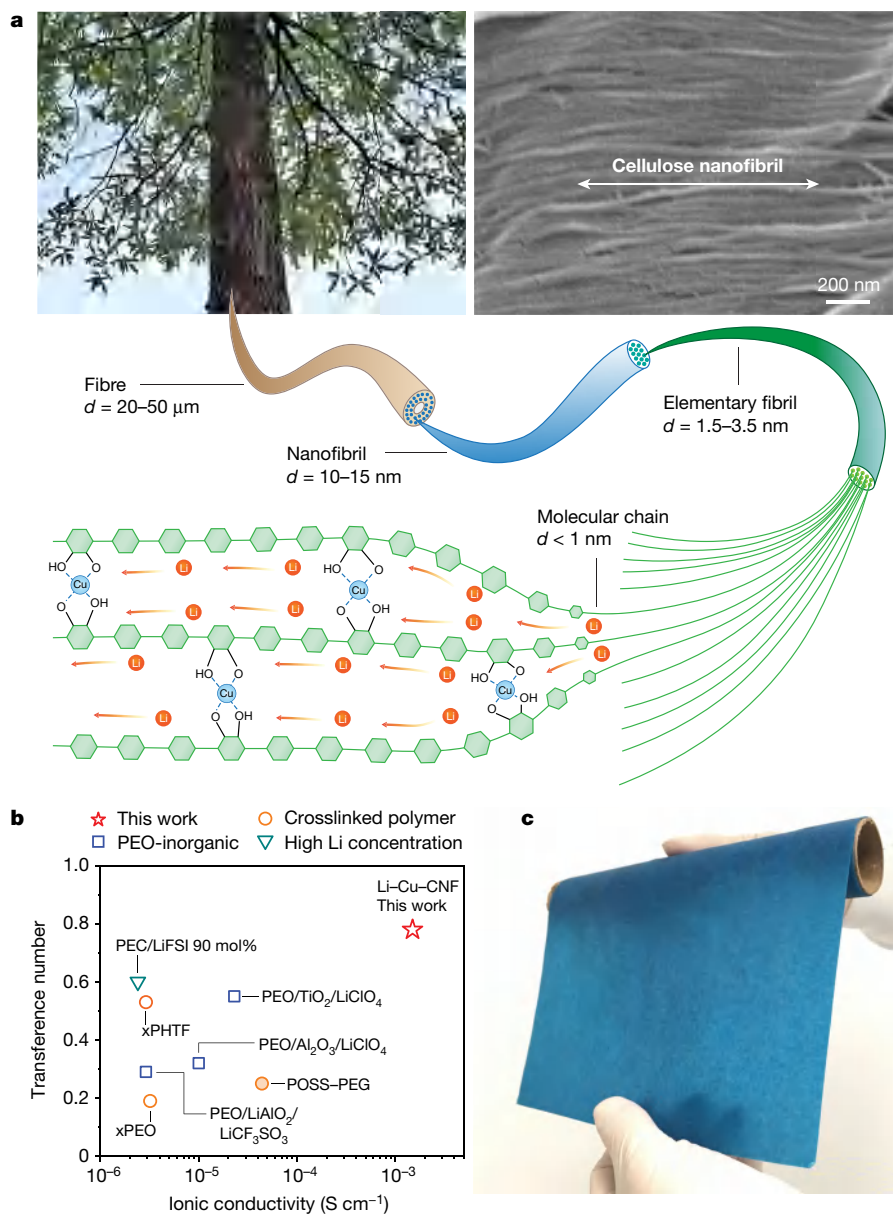
Chunpeng Yang<sup>1,13</sup>, Qisheng Wu<sup>2,13</sup>, Weiqi Xie<sup>1,13</sup>, Xin Zhang<sup>1</sup>, Alexandra Brozena<sup>1</sup>, Jin Zheng<sup>3</sup>, Mounesha N. Garaga<sup>4</sup>, Byung Hee Ko<sup>5</sup>, Yimin Mao<sup>1,6</sup>, Shuaiming He<sup>1</sup>, Yue Gao<sup>1</sup>, Pengbo Wang<sup>3</sup>, Madhusudan Tyagi<sup>1,6</sup>, Feng Jiao<sup>5</sup>, Robert Briber<sup>1</sup>, Paul Albertus<sup>7</sup>, Chunsheng Wang<sup>7</sup>, Steven Greenbaum<sup>4</sup>, Yan-Yan Hu<sup>3,8</sup>, Akira Isogai<sup>9</sup>, Martin Winter<sup>10</sup>, Kang Xu<sup>11</sup>, Yue Qi<sup>2,13</sup> & Liangbing Hu<sup>1,12</sup>✉

Although solid-state lithium (Li)-metal batteries promise both high energy density and safety, existing solid ion conductors fail to satisfy the rigorous requirements of battery operations. Inorganic ion conductors allow fast ion transport, but their rigid and brittle nature prevents good interfacial contact with electrodes. Conversely, polymer ion conductors that are Li-metal-stable usually provide better interfacial compatibility and mechanical tolerance, but typically suffer from inferior ionic conductivity owing to the coupling of the ion transport with the motion of the polymer chains<sup>1–3</sup>. Here we report a general strategy for achieving high-performance solid polymer ion conductors by engineering of molecular channels. Through the coordination of copper ions (Cu<sup>2+</sup>) with one-dimensional cellulose nanofibrils, we show that the opening of molecular channels within the normally ion-insulating cellulose enables rapid transport of Li<sup>+</sup> ions along the polymer chains. In addition to high Li<sup>+</sup> conductivity (1.5 × 10<sup>−3</sup> siemens per centimetre at room temperature along the molecular chain direction), the Cu<sup>2+</sup>-coordinated cellulose ion conductor also exhibits a high transference number (0.78, compared with 0.2–0.5 in other polymers<sup>2</sup>) and a wide window of electrochemical stability (0–4.5 volts) that can accommodate both the Li-metal anode and high-voltage cathodes. This one-dimensional ion conductor also allows ion percolation in thick LiFePO<sub>4</sub> solid-state cathodes for application in batteries with a high energy density. Furthermore, we have verified the universality of this molecular-channel engineering approach with other polymers and cations, achieving similarly high conductivities, with implications that could go beyond safe, high-performance solid-state batteries.

Solid-state batteries with lithium-metal anodes are attractive as next-generation energy-storage systems with high energy density and safety. The realization of such batteries will depend largely on the development of superior ion conductors for the solid-state electrolyte and of an ion-conducting network for the cathode materials. Solid polymer electrolytes (SPEs)—typically ether-based, such as poly(ethylene oxide) (PEO)<sup>3,4</sup>—are promising candidates, owing to their low density, ability to dissociate Li salts at elevated temperatures, facile processibility, and good interfacial contact with the electrodes<sup>5–7</sup>. However, Li<sup>+</sup> transport in SPEs is highly coupled with the segmental motion of the polymer chains, resulting in limited ionic conductivities (generally less than 10<sup>−5</sup> S cm<sup>−1</sup> at room temperature<sup>2</sup>) and low Li<sup>+</sup>-transference numbers (usually 0.2–0.5)<sup>8,9</sup>.

To improve the conductivity of Li<sup>+</sup> ions, SPEs are commonly used at elevated temperatures in order to promote the segmental motion of the polymer for faster ion movement. However, increasing the temperature deteriorates the mechanical strength of the SPE and compromises the safety of the battery. Other efforts to improve the Li<sup>+</sup> conductivity, transference number and/or mechanical properties of SPEs include modifying the polymer matrix structure with crosslinked polymers<sup>10–12</sup>, block copolymers<sup>13</sup> and single-ion-conducting polymers<sup>14</sup>, or incorporating inorganic fillers<sup>4,15,16</sup>. Despite these approaches, the tradeoff between the ion conduction, transference number and mechanical strength in SPEs has persisted for more than four decades, and the room-temperature ionic conductivity of SPEs barely approaches

<sup>1</sup>Department of Materials Science and Engineering, University of Maryland, College Park, MD, USA. <sup>2</sup>School of Engineering, Brown University, Providence, RI, USA. <sup>3</sup>Department of Chemistry and Biochemistry, Florida State University, Tallahassee, FL, USA. <sup>4</sup>Department of Physics and Astronomy, Hunter College, City University of New York, New York, NY, USA. <sup>5</sup>Center for Catalytic Science and Technology, Department of Chemical and Biomolecular Engineering, University of Delaware, Newark, DE, USA. <sup>6</sup>NIST Center for Neutron Research, National Institute of Standards and Technology (NIST), Gaithersburg, MD, USA. <sup>7</sup>Chemical and Biomolecular Engineering, University of Maryland, College Park, MD, USA. <sup>8</sup>Center of Interdisciplinary Magnetic Resonance, National High Magnetic Field Laboratory, Tallahassee, FL, USA. <sup>9</sup>Laboratory of Cellulose Chemistry, Department of Biomaterial Sciences, The University of Tokyo, Tokyo, Japan. <sup>10</sup>MEET Battery Research Center, Institute of Physical Chemistry, University of Münster, Münster, Germany. <sup>11</sup>Battery Science Branch, Energy Science Division, Sensor and Electron Devices Directorate, Army Research Laboratory, Adelphi, MD, USA. <sup>12</sup>Center for Materials Innovation, University of Maryland, College Park, MD, USA. <sup>13</sup>These authors contributed equally: Chunpeng Yang, Qisheng Wu, Weiqi Xie. ✉e-mail: yueqi@brown.edu; binghu@umd.edu



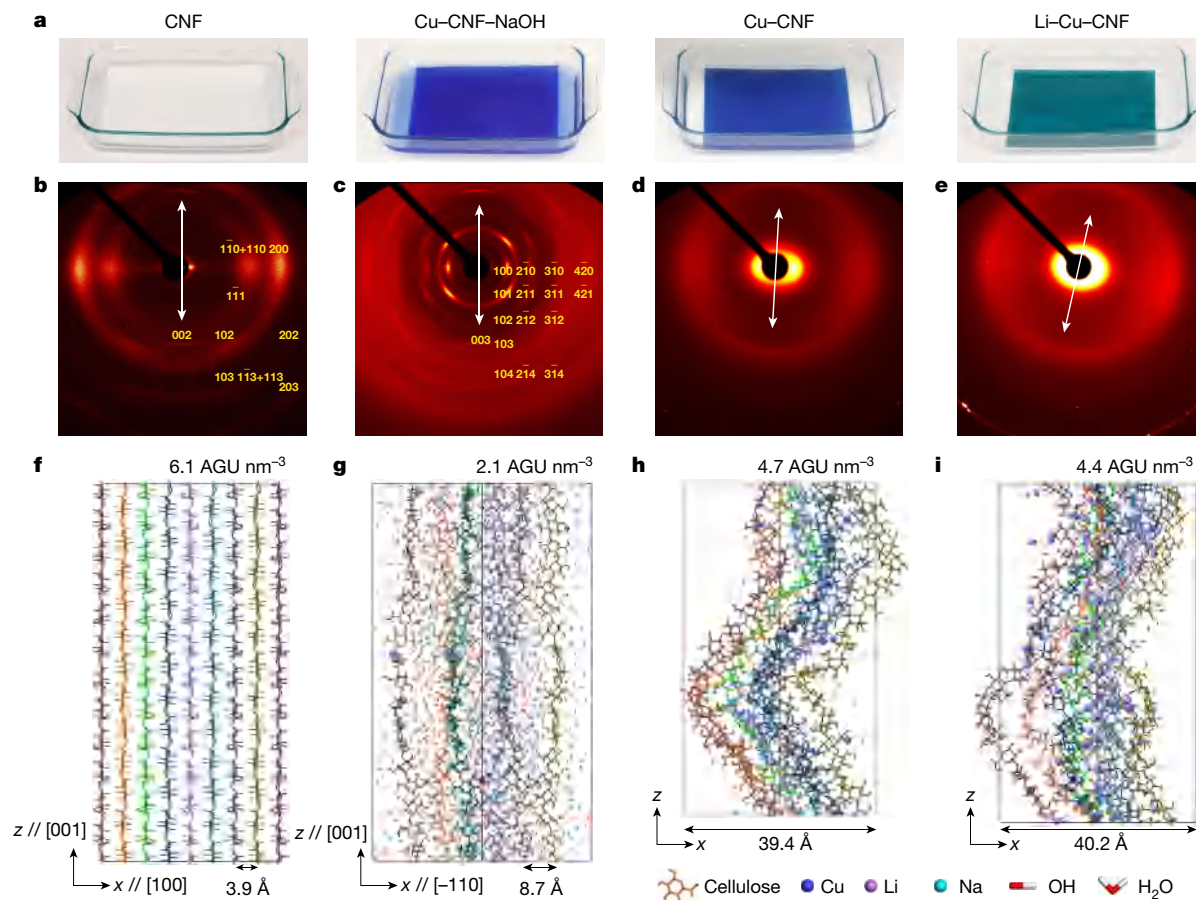
**Fig. 1 | Structure and ion-transport performance of the Li-Cu-CNF solid-state ion conductor.** **a**, Bottom, schematic illustration of the hierarchical structure of CNFs, which are derived from wood cellulose fibres and are composed of elementary fibrils, each of which comprises individual cellulose molecular chains. Coordination of  $\text{Cu}^{2+}$  ions with the hydroxyl groups of cellulose opens the spacing between the molecular chains, creating cellulose molecular channels in the CNFs that serve as  $\text{Li}^+$ -conducting pathways in the resulting Li-Cu-CNF ion conductor. The scanning electron microscopy (SEM)

image at the top right shows the morphology of the CNFs, which are naturally aligned in the cellulose fibres. **b**, Transference number is plotted against  $\text{Li}^+$  ionic conductivity for Li-Cu-CNF (along the direction of its cellulose chains) and for other SPEs (which are gel/liquid-free and stable against Li metal), including PEO-inorganic composites (squares, ref. <sup>15</sup>), crosslinked polymers (unfilled circles, ref. <sup>11</sup>; filled circles, ref. <sup>12</sup>), and a high-Li-concentration electrolyte (triangles, ref. <sup>26</sup>). **c**, Digital photo of a 1-m-long roll of Li-Cu-CNF membrane.

$10^{-4} \text{ S cm}^{-1}$ . Additionally, SPEs feature poor ionic percolation when used as ion-conducting additives in cathode materials, requiring a threshold content of roughly 25 wt% SPE<sup>17,18</sup>, which further reduces the energy density of the battery. Clearly, the conventional SPE structure and  $\text{Li}^+$ -transport mechanism must be drastically transformed to meet future energy-storage needs.

Here, we explore a design strategy for polymer ion conductors that is based on expanding the intermolecular polymer structure and decoupling the  $\text{Li}^+$  transport from the polymer segmental relaxation, which leads to high ionic conductivity. We first demonstrate this approach using cellulose nanofibrils (CNFs, either as individual building blocks or as an integral component in the format of paper or delignified wood). CNFs are abundantly available from various biomass sources

(for example, wood) and feature an aligned, one-dimensional (1D) hierarchical structure rich in oxygen-containing polar functional groups (for example, hydroxyl) in the form of repeating anhydroglucose units (AGUs) that make up the cellulose molecular chains (Fig. 1a). Such polar functionalities could solvate  $\text{Li}^+$  and aid in  $\text{Li}^+$  movement. However, the narrow spacing between the cellulose molecular chains does not naturally allow  $\text{Li}^+$  incorporation. As a result, CNFs have been used previously only as an inert supporting matrix for liquid/gel electrolytes (not a solid-state ion conductor) or other SPEs (with poor ionic conductivities)<sup>19-21</sup>. We show here that the coordination of copper ions ( $\text{Cu}^{2+}$ ) with CNFs (producing Cu-CNF) allows us to alter the crystalline structure of the cellulose by expanding the spacing between the polymer chains into molecular channels that enable the insertion and



**Fig. 2 | Structural evolution during the synthesis of Li-Cu-CNF.** **a**, Digital images showing the process of fabricating Li-Cu-CNF, during which the CNF paper is immersed in  $\text{Cu}^{2+}$  alkaline solution to produce Cu-CNF-NaOH. The aqueous solution in Cu-CNF-NaOH is then displaced with DMF to obtain the Cu-CNF membrane, and finally exchanged with  $\text{LiPF}_6$  organic electrolyte for  $\text{Li}^+$  insertion and then dried to form the Li-Cu-CNF membrane. **b–e**, Fibre XRD patterns for pristine CNFs (naturally aligned in densified wood), showing a cellulose  $\text{I}_\beta$  structure (**b**); Cu-CNF-NaOH, with coordinated cellulose chains packed in a hexagonal unit-cell structure consistent with the literature<sup>23</sup> (**c**); Cu-CNF, in a largely amorphous state (**d**); and Li-Cu-CNF, which features an

rapid transport of  $\text{Li}^+$  ions (Fig. 1a). In such 1D conduction passages, the abundant oxygen-containing functional groups of cellulose, along with a small amount of bound water, assist in the movement of  $\text{Li}^+$  in a manner that is decoupled from the segmental motion of the polymer.

As a result, the  $\text{Li}^+$ -inserted Cu-CNF (Li-Cu-CNF) ion conductor features a high ionic conductivity of  $1.5 \times 10^{-3} \text{ S cm}^{-1}$  (10–1000 times that of other Li-stable SPEs) and a high transference number of 0.78 at room temperature (Fig. 1b). Li-Cu-CNF also features a wide electrochemical stability window of 0–4.5 V (potentials in this work are all versus  $\text{Li}^+/\text{Li}$ ), in addition to low cost, scalability and flexibility (Fig. 1c). Besides serving as a thin and dense solid-state separator/electrolyte, the 1D structure of Li-Cu-CNF also makes it an effective ion-conducting binder for thick solid-state electrodes in which low ionic conductivity has been a key hurdle. Indeed, the effective ionic percolation of Li-Cu-CNF has allowed us to fabricate a thick  $\text{LiFePO}_4$  solid-state cathode (roughly 120  $\mu\text{m}$ ), suggesting the material's potential for increasing battery energy density. This design principle—using facile coordination chemistry and expansion of the polymer molecular channels to provide fast diffusion pathways for uncoupled  $\text{Li}^+$  transport—can be applied to other polymers and cations, enabling high-performance solid-state ion conductors that may have applications far beyond high-energy-density and safe solid-state batteries.

amorphous structure (with some weak diffraction signals characteristic of cellulose II; ref. <sup>22</sup>) (**e**). The white arrows in the fibre XRD patterns indicate the fibre direction. **f–i**, Simulated structures of CNFs (**f**), Cu-CNF-NaOH (**g**), Cu-CNF (**h**) and Li-Cu-CNF materials (**i**) (see Extended Data Fig. 2d–g for more details of the simulated structures). Different cellulose chains in the simulated structures are denoted by different colours. In **f**, **g**, the  $x$  and  $z$  axes are parallel to specific directions (for example,  $z // [001]$  means the  $z$  axis is parallel to the  $[001]$  direction); in **h**, **i**, the structures are amorphous and there is no crystal direction.

## Synthesis and structure analysis

We fabricated the solid-state Li-Cu-CNF ion conductor using a simple ion-coordination and solvent-exchange process (Fig. 2a). We first immersed the CNF-containing materials (for example, CNF suspensions, cellulose paper, or aligned CNFs derived from wood, as specified in the Methods) in  $\text{Cu}^{2+}$ -saturated alkaline solution (20% NaOH), in which  $\text{Cu}^{2+}$  gradually coordinates with the cellulose molecular chains, forming a blue-coloured Cu-CNF-NaOH complex filled with NaOH solution. After washing the NaOH from Cu-CNF-NaOH with water, displacing the water with dimethylformamide (DMF), and finally evaporating the DMF under vacuum, we obtained the solid-state Cu-CNF material.  $\text{Li}^+$  was then inserted into the Cu-CNF by soaking in an electrolyte consisting of  $\text{LiPF}_6$  in non-aqueous solvents, followed by evaporation of the solvents, producing the Li-Cu-CNF ion conductor (Fig. 2a and Supplementary Discussion 1 in the Supplementary Information).

We applied fibre X-ray diffraction (XRD; Fig. 2b–e and Extended Data Fig. 1a–d) and X-ray absorption spectroscopy (XAS; Extended Data Fig. 1e–h) to track the structural evolution during the fabrication process. We also constructed model structures of the materials through molecular dynamics (MD) simulations (Fig. 2f–i; for details, see Methods and Extended Data Fig. 2), using the fibre XRD results. The pristine

CNFs feature a typical monoclinic diffraction pattern of cellulose I<sub>β</sub>, with diffraction peaks at (110), (200) and so on (Fig. 2b), showing a cellulose molecular spacing ( $d_{200}$ ) of 0.39 nm<sup>22</sup>. The corresponding MD simulation of the crystalline CNF (Fig. 2f) suggests that the material cannot accommodate the insertion of Li<sup>+</sup> between the intermolecular spacing owing to the close packing of the cellulose chains. By contrast, the Cu–CNF–NaOH features a hexagonal crystal structure, with three-fold symmetry along the direction of the cellulose chains (Fig. 2c)<sup>23</sup>. In the simulated structure of the Cu–CNF–NaOH (Fig. 2g), each cellulose chain has three neighbouring chains, with an interchain distance of 0.87 nm, which are bridged by Cu<sup>2+</sup> via four coordinated Cu–O bonds, opening the close molecular packing of the CNFs. After removing NaOH and liquid water, the crystalline Cu–CNF–NaOH becomes amorphous Cu–CNF (Fig. 2d). This amorphous structure has a much lower density of cellulose packing (4.7 AGU nm<sup>-3</sup>; Fig. 2h) than do the pristine CNFs (6.1 AGU nm<sup>-3</sup>; Fig. 2f), with molecular channels opened between the cellulose chains. The final Li–Cu–CNF structure after Li<sup>+</sup> is inserted into these channels maintains the amorphous state (Fig. 2e) with a low packing density (4.4 AGU nm<sup>-3</sup>; Fig. 2i). XAS (Extended Data Fig. 1e–h) further confirms that the Cu<sup>2+</sup> ions are bonded with O atoms in the amorphous Cu–CNF and Li–Cu–CNF materials, with an average bonding distance of 1.97 Å. As a result of the coordination of Cu<sup>2+</sup>, the amorphous Li–Cu–CNF has expanded molecular channels that can accommodate Li<sup>+</sup>.

### Li<sup>+</sup> conduction in Li–Cu–CNF

The Li–Cu–CNF material contains a small amount of bound water but still displays excellent electrochemical stability. <sup>1</sup>H magic-angle spinning (MAS) nuclear magnetic resonance (NMR; Extended Data Fig. 3a, b) shows that the final Li–Cu–CNF product contains roughly 1.9 wt% of H<sub>2</sub>O (lower than the 4–6 wt% typically found in regular paper<sup>24</sup>). This small amount of water in Li–Cu–CNF does not aggregate as a condensed liquid phase, but instead exists as discrete H<sub>2</sub>O molecules bound to the cellulose through hydrogen bonding, as shown by Fourier-transform infrared spectra (FTIR), quasi-elastic neutron scattering (QENS) and differential scanning calorimetry (DSC), as well as model simulations (Extended Data Fig. 3c–h). The low content of bound water in Li–Cu–CNF does not compromise the material's solid nature, but is essential for its flexibility (Fig. 1c) and high mechanical strength (29.2 MPa; Extended Data Fig. 3i). More importantly, Li–Cu–CNF containing bound water still has a wide electrochemical stability window of 0–4.5 V (Fig. 3a and Extended Data Fig. 4), which allows for the reversible operation of the Li-metal anode and high-voltage cathodes (for example, LiNi<sub>0.8</sub>Mn<sub>0.1</sub>Co<sub>0.1</sub>O<sub>2</sub> (NMC811)) needed for high-energy-density solid-state batteries. This is substantially different from electrolytes that contain free liquid water<sup>25</sup>, where the water molecules exist as bulk liquid and hence are reactive with Li metal.

The Li–Cu–CNF material serves as an excellent Li<sup>+</sup> conductor. At 25 °C, Li–Cu–CNF has a high Li<sup>+</sup> conductivity of  $1.5 \times 10^{-3} \text{ S cm}^{-1}$  along the direction of the cellulose molecular chains (that is, in the fibre direction; Extended Data Fig. 5a–d), which is higher by orders of magnitude than that of other reported SPEs (Fig. 3b)<sup>3,4,10,11,13,14,17,26</sup>. The conductivity–temperature relationship of Li–Cu–CNF (along the fibre direction) follows an Arrhenius-type behaviour (that is, logarithmic conductivity linear to  $1/T$ ). According to the Arrhenius equation, the activation energy is 0.19 eV, which is much lower than that of PEO (roughly 1 eV)<sup>3</sup> and PEO–inorganic composite electrolytes (roughly 0.6 eV)<sup>4</sup>. Additionally, a Li–Cu–CNF paper electrolyte consisting of three-dimensionally, randomly distributed Li–Cu–CNF shows a through-plane ionic conductivity of  $3.4 \times 10^{-4} \text{ S cm}^{-1}$  at room temperature—still much higher than that of all reported Li-stable SPEs (Fig. 3b)<sup>3,4,10,11,13,14,17,26</sup>. The through-plane conductivity–temperature relationship also follows the Arrhenius equation, without a transition point even at temperatures below 0 °C (Fig. 3b and Extended Data Fig. 5e–g). Li–Cu–CNF offers a similar ionic conductivity

to oxide-based electrolytes (for example, Li<sub>3</sub>La<sub>2</sub>Zr<sub>2</sub>O<sub>12</sub> (LLZO)) but at a much lower Li concentration ( $1.2 \text{ mol l}^{-1}$  versus  $41.3 \text{ mol l}^{-1}$  in LLZO<sup>27</sup>; Fig. 3c), which is preferential for lower cost. The Li concentration is similar to that of PEO (roughly  $1.1 \text{ mol l}^{-1}$ )<sup>27</sup>, but Li–Cu–CNF features a roughly 500 times higher Li<sup>+</sup> diffusion coefficient at room temperature ( $D_{\text{Li}} = 6.1 \times 10^{-7} \text{ cm}^2 \text{ s}^{-1}$ , by <sup>7</sup>Li pulsed field gradient (PFG) NMR; Supplementary Discussion 2).

The Cu<sup>2+</sup> in Li–Cu–CNF is not mobile, as indicated by a negligible Cu<sup>2+</sup> conductivity of  $1.0 \times 10^{-8} \text{ S cm}^{-1}$  (Extended Data Fig. 5h), but it does have an indispensable role in opening the cellulose molecular channels to allow transport of Li<sup>+</sup> in Li–Cu–CNF. Without Cu<sup>2+</sup> coordination, the control sample Li–CNF (synthesized similarly to Li–Cu–CNF but in the absence of Cu<sup>2+</sup>) has closely packed cellulose chains that spatially prevent Li<sup>+</sup> from accessing the interior of the nanofibrils (Extended Data Fig. 5n) and thus displays a much lower Li<sup>+</sup> conductivity (Fig. 3b). In addition, Li–Cu–CNF shows a high Li<sup>+</sup> transference number of 0.78 (Extended Data Fig. 5i, j), which is much higher than that of Li–CNF (0.35; Extended Data Fig. 5k–m) and other SPEs (0.2–0.5; Fig. 1b), except single-Li-ion conducting polymers<sup>13,14</sup> (which feature a transference number of close to 1.0, although this is often achieved at the impractical expense of the overall ionic conductivity).

In the Li–Cu–CNF molecular channels, the Li<sup>+</sup> can form multiple coordinations with the rich oxygen-containing functional groups (shown schematically in Fig. 3d), including hydroxyl (ROH), carboxylate (COO<sup>-</sup>), alkoxide (RO<sup>-</sup>), and ether (EO) moieties, in addition to bound H<sub>2</sub>O molecules and some residual PF<sub>6</sub><sup>-</sup>. Given the Li<sup>+</sup> content (1.3 wt%) in Li–Cu–CNF measured by inductively coupled plasma (ICP) analysis, the number of oxygen atoms is roughly 20 times that of Li<sup>+</sup>. Solid-state <sup>6</sup>Li NMR (Extended Data Fig. 6a–d) shows that the number of Li<sup>+</sup> ions that are coordinated with oxygen atoms (RO⋯Li, COO⋯Li, and ROH/H<sub>2</sub>O⋯Li) in the Li–Cu–CNF material is substantially larger than that in Li–CNF. MD simulations also reveal that the Li–O coordination number in Li–Cu–CNF (4.2), due to Li<sup>+</sup> insertion, is much larger than that in Li–CNF (3.0), due to surface adsorption (Fig. 3e). The multiple Li–O coordination is important for the diffusion of Li<sup>+</sup>. When Li<sup>+</sup> moves, it can dissociate from just one to two bonded oxygen atoms while still coordinating with the others, resulting in a low hopping energy barrier<sup>28</sup>.

To investigate the Li<sup>+</sup>-transport pathways, we performed <sup>6</sup>Li tracer-exchange NMR (Extended Data Fig. 6e–g)<sup>29</sup>. After <sup>7</sup>Li in Li–Cu–CNF was exchanged with <sup>6</sup>Li tracer by electrochemical cycling, the number of <sup>6</sup>Li<sup>+</sup> ions coordinated with COO<sup>-</sup>, RO<sup>-</sup>, ROH/H<sub>2</sub>O and PF<sub>6</sub><sup>-</sup> in Li–Cu–CNF increased by 15, 20, 25 and 4.5 times, respectively, compared with Li–Cu–CNF before cycling (Fig. 3f and Extended Data Fig. 6g). Thus, the hopping sites of Li<sup>+</sup> are mainly the counter-anions in the cellulose (COO<sup>-</sup> and RO<sup>-</sup>).

MD simulations further show that the Li<sup>+</sup> in Li–Cu–CNF hops between the COO<sup>-</sup> and RO<sup>-</sup> sites instead of moving within a solvation sheath formed by the polymer chain segment (Extended Data Fig. 7a), with the assistance of H<sub>2</sub>O molecules (Extended Data Fig. 7b, c). The rich oxygen groups in Li–Cu–CNF (COO<sup>-</sup>, RO<sup>-</sup>, ROH, and EO) form a continuous Li<sup>+</sup>-hopping pathway, with a short hopping distance (roughly 3.0 Å; Extended Data Fig. 7d) close to that of fast inorganic ion conductors<sup>30</sup>, enabling high-mobility Li<sup>+</sup> hopping. The counter-anions in the cellulose (COO<sup>-</sup> and RO<sup>-</sup>) move much less than Li<sup>+</sup> (Extended Data Fig. 7e), while the only mobile counter-anion is the residual PF<sub>6</sub><sup>-</sup>, resulting in the high transference number of Li–Cu–CNF (0.78; see Supplementary Discussion 2 for more analysis). Figure 3g shows a simulated fast-moving Li<sup>+</sup> ion travelling along or between the cellulose molecular chains, while the cellulose backbone moves very little, indicating that the Li<sup>+</sup> hopping is decoupled from the motion of the polymer chain. This decoupled Li<sup>+</sup>-hopping mechanism—which is enabled jointly by the open molecular channels, multiple Li–O coordination and assistance of bound water molecules—contributes to the unprecedentedly high ionic conductivity and transference number of Li–Cu–CNF.



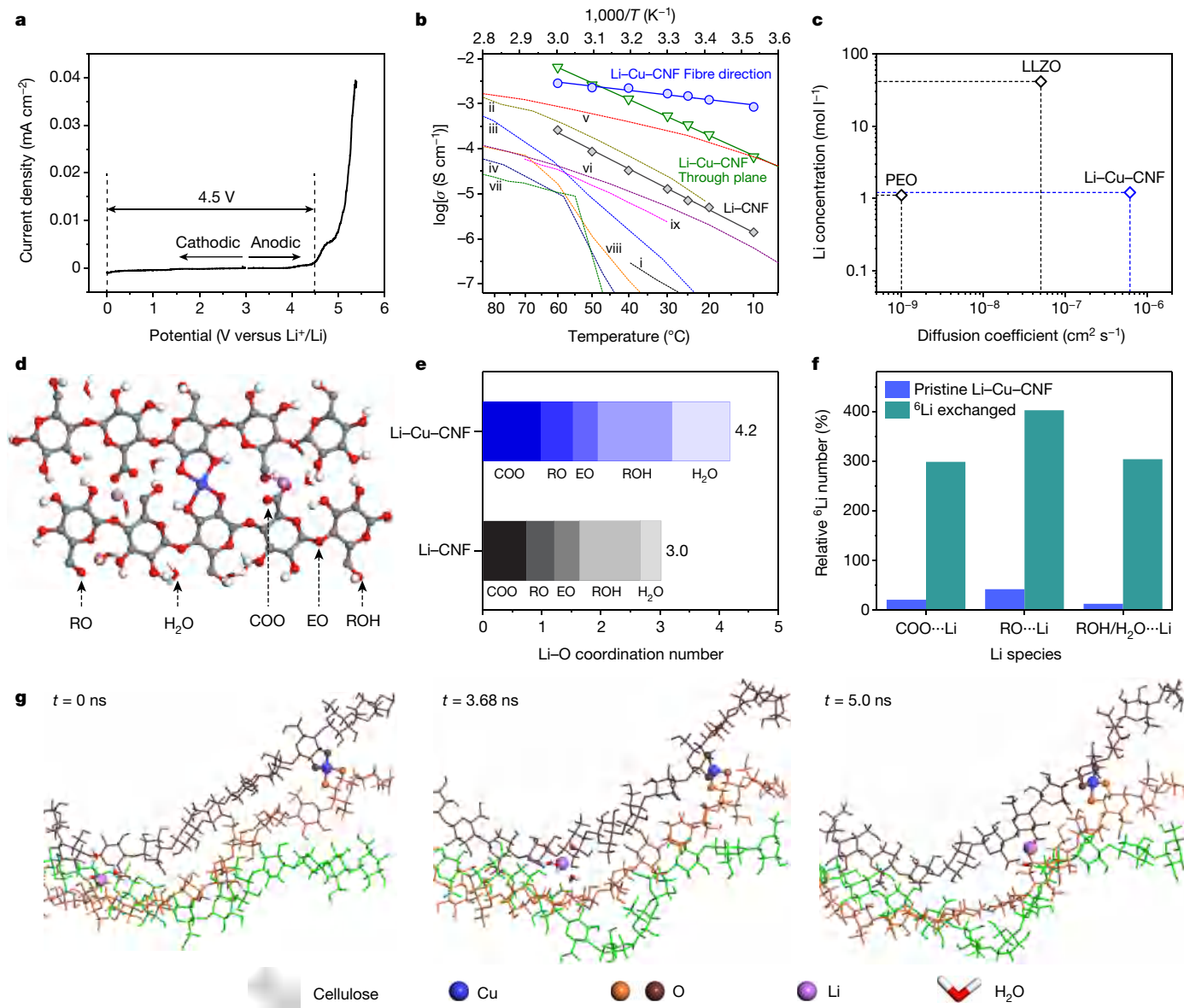


**Fig. 3 | Li<sup>+</sup> conductivity and transport mechanism in Li-Cu-CNF.** **a**, Linear sweep voltammetry (LSV) of Li-Cu-CNF measured at 0.1 mV s<sup>-1</sup> (cathodic scan from open-circuit voltage (OCV) to 0 V; anodic scan from OCV to 5.4 V). The electrochemical stability window is 0–4.5 V, in which the current density is 10<sup>-6</sup> A cm<sup>-2</sup> or less. **b**, Temperature-dependent conductivity of Li-Cu-CNF (along the direction of the CNF fibre and through the plane of a randomly distributed Li-Cu-CNF paper electrolyte) and Li-CNF (without Cu<sup>2+</sup> coordination), with linear fitting according to the Arrhenius equation, the slope of which indicates the activation energy. Temperature-dependent conductivity plots (i–ix) for typical SPEs (which are gel/liquid-free and stable against Li metal) are included for comparison, including PEO (i, ref. <sup>3</sup>), PEO-inorganic composites (ii–iv, ref. <sup>4</sup>), crosslinked polymers (v, ref. <sup>10</sup>; vi, ref. <sup>11</sup>), single-ion-conducting polymers (vii, ref. <sup>13</sup>; viii, ref. <sup>14</sup>), and

high-Li-concentration electrolytes (ix, ref. <sup>26</sup>). **c**, Comparison of the Li<sup>+</sup> diffusion coefficient and Li<sup>+</sup> concentration of Li-Cu-CNF with other solid-state electrolytes (PEO and LLZO). **d**, Diagram showing the chemical environment of Li<sup>+</sup> in the Li-Cu-CNF system with different types of oxygen atom. C, H, O, Cu and Li atoms are denoted with grey, white, red, blue and purple spheres, respectively. The hydrogen atoms that are bonded with carbon are not shown for clarity. **e**, Average Li-O coordination numbers from MD simulations of Li-CNF and Li-Cu-CNF. **f**, Relative <sup>6</sup>Li numbers for different Li chemical environments in Li-Cu-CNF before and after <sup>6</sup>Li → <sup>7</sup>Li tracer exchange, derived from <sup>6</sup>Li NMR (Extended Data Fig. 6). **g**, Structural snapshots from MD simulations of a fast-moving Li<sup>+</sup> ion transporting in Li-Cu-CNF, with a displacement of 18.8 Å in 5 ns.

### Use of Li-Cu-CNF in batteries

The 1D, nanoscale Li-Cu-CNF ion conductor can be applied as both an independent solid-state electrolyte and an effective ion-conducting binder for constructing continuous Li<sup>+</sup>-transport networks in solid-state cathodes (Fig. 4a), both of which are crucial for building high-performance solid-state Li-metal batteries. We first show that Li-Cu-CNF can be assembled and pressed into a thin (roughly 50 μm) yet dense paper with three-dimensionally, randomly distributed

fibrils (Fig. 4b and Extended Data Fig. 8a, b) as a solid-state electrolyte. The Li-Cu-CNF electrolyte enables stable Li-cycling performance at 0.5 mA cm<sup>-2</sup> for 300 h in a Li-metal symmetric cell without dendrite-induced short-circuiting or Cu<sup>2+</sup> reduction on Li (Extended Data Fig. 8c–e), indicating the compatibility of Li-Cu-CNF with a Li-metal anode.

We also applied individual Li-Cu-CNF fibrils as an effective ion-conducting binder for thick battery electrodes in order to overcome interfacial ion-transport challenges. As an ion-conducting binder,

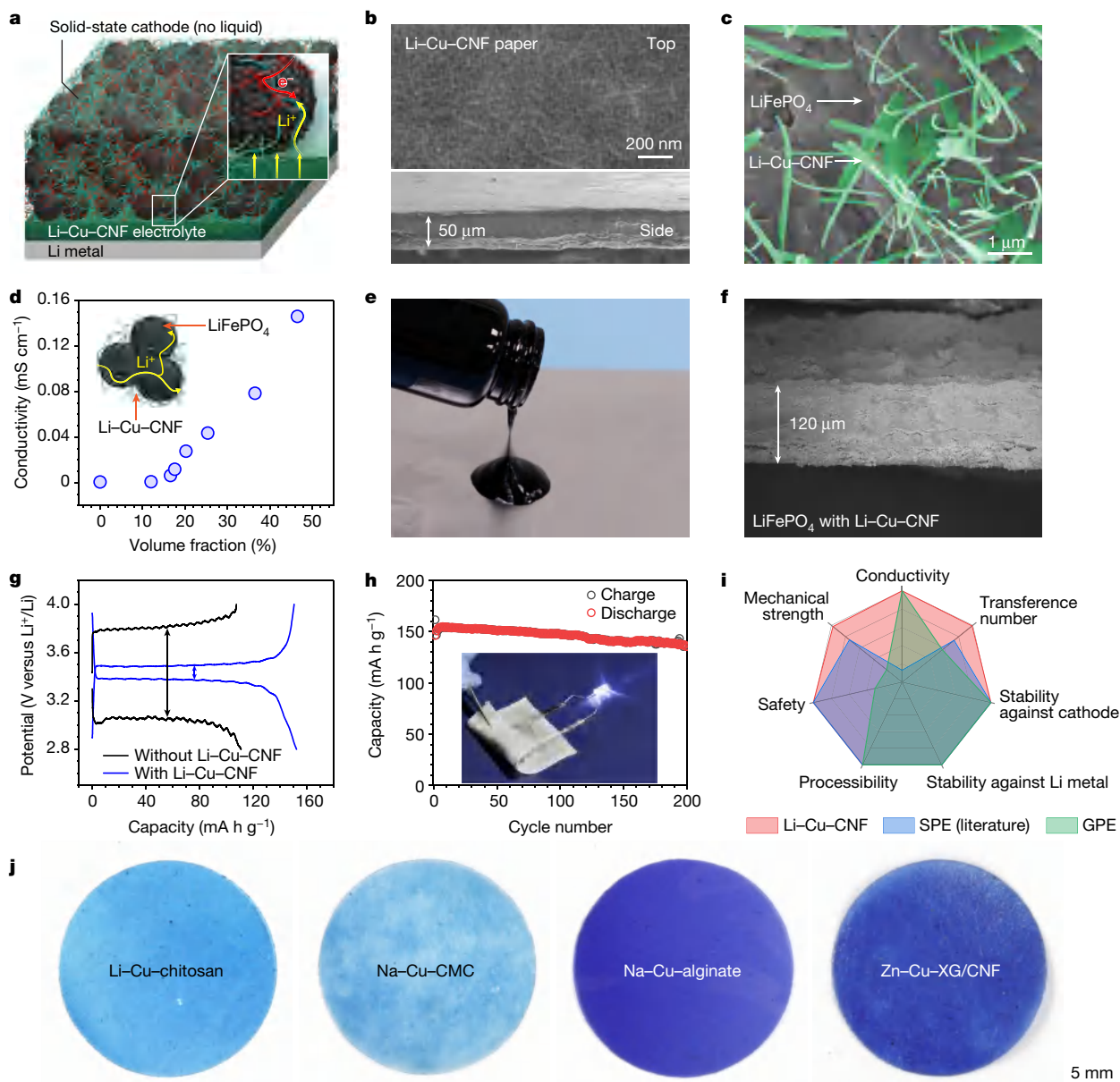


**Fig. 4 | Demonstration of solid-state Li metal batteries using the Li-Cu-CNF ion conductor.** **a**, Diagram of a solid-state full battery consisting of a Li-metal anode, the Li-Cu-CNF paper electrolyte and the solid-state cathode (black spheres) featuring the Li-Cu-CNF as an ion-conducting binder (green fibres). The Li-Cu-CNF enables transport of  $\text{Li}^+$  ions (yellow arrows), and carbon nanotubes (CNTs, red fibres) in the cathode enable electron ( $e^-$ ) transport (red arrow). **b**, Top-view (top) and side-view (bottom) SEM images of the dense Li-Cu-CNF paper electrolyte. **c**, SEM image of the  $\text{LiFePO}_4$  cathode with the Li-Cu-CNF ion-conducting additive (false colour: grey,  $\text{LiFePO}_4$ ; green, Li-Cu-CNF). **d**, Ionic conductivity of  $\text{LiFePO}_4$  cathodes made with different amounts of Li-Cu-CNF to achieve ionic percolation. **e**, Photograph of the cathode slurry, consisting of  $\text{LiFePO}_4$  and the Cu-CNF additive, for casting the electrode and subsequent  $\text{Li}^+$  insertion. **f**, Cross-sectional SEM image of a 120- $\mu\text{m}$ -thick  $\text{LiFePO}_4$  cathode made using Li-Cu-CNF and CNT additives.

**g**, Galvanostatic charge/discharge voltage profiles of thick  $\text{LiFePO}_4$  solid-state cathodes made with or without Li-Cu-CNF ion-conducting binder. The arrows indicate the overpotentials at half capacity. **h**, Cycle performance of a solid-state  $\text{LiFePO}_4$  cell made using Li-Cu-CNF ion-conducting binder in the cathode, Li-Cu-CNF electrolyte, and a Li-metal anode. Inset, digital photograph of the folded solid-state battery based on the  $\text{LiFePO}_4$  cathode and Li-Cu-CNF. **i**, Performance of the Li-Cu-CNF electrolyte compared with SPEs and gel polymer electrolytes (GPEs) reported in the literature. The spider chart indicates the top performance for each parameter in the field, not the combined performance of any specific SPE or GPE (see Supplementary Discussion 7 for details). **j**, Digital photos of M-Cu-polymer electrolytes (analogues of Li-Cu-CNF), where M = Li, Na or Zn, and the polymers include chitosan, carboxymethyl cellulose (CMC), alginate acid and xanthan gum (XG)/CNF.

Li-Cu-CNF has the advantage of the high aspect ratio (roughly 200) of the CNFs, which should enable a low percolation threshold<sup>31</sup>. We selected  $\text{LiFePO}_4$  to demonstrate that the incorporation of 1D Li-Cu-CNF additive forms an ion-percolation network within the solid-state cathode (Fig. 4c). The resulting cathode featured a percolation threshold of 15 vol% to form an ion-conducting network (Fig. 4d), which corresponds to roughly 5 wt% of the Li-Cu-CNF additive in the composite (Supplementary

Discussion 3). Moreover, the use of the Li-Cu-CNF ion-conducting binder is compatible with the traditional slurry-casting method for electrode preparation (Fig. 4e and Extended Data Fig. 9a), which allows large-scale, roll-to-roll manufacturing of solid-state batteries.

We further show the effective  $\text{Li}^+$  transport enabled by Li-Cu-CNF in a full battery featuring both the Li-Cu-CNF paper electrolyte and a thick (120  $\mu\text{m}$ ) solid-state  $\text{LiFePO}_4$  cathode containing the Li-Cu-CNF

additive. The solid-state LiFePO<sub>4</sub> cathode (Fig. 4f) demonstrated here is three to five times thicker than other reported solid-state LiFePO<sub>4</sub> cathodes<sup>11,17,18,32</sup>. With the Li–Cu–CNF ion-conducting binder, this thick LiFePO<sub>4</sub> cathode showed much smaller impedance (Extended Data Fig. 9b, c), reduced overpotential and higher capacity (Fig. 4g) compared with the cathode without the Li–Cu–CNF binder. The solid-state LiFePO<sub>4</sub> battery with Li–Cu–CNF also showed good cycling performance with a capacity retention of 94% after 200 cycles at room temperature (Fig. 4h), which cannot be achieved with a PEO electrolyte (Supplementary Discussion 4). The disassembled cells after cycling showed that Li–Cu–CNF is stable against the Li metal and cathode, without Cu<sup>2+</sup> reduction on the Li-metal anode (Supplementary Discussion 5, 6). The flexibility of the Li–Cu–CNF electrolyte also allowed us to fabricate a flexible solid-state battery that remained operational when folded (Fig. 4h, inset, and Extended Data Fig. 9d).

The stability of Li–Cu–CNF against the Li-metal anode and high-voltage cathode materials enables its use in high-energy-density solid-state batteries. As a proof-of-concept, we successfully demonstrated long-term cycling of solid-state batteries constructed using a Li-metal anode, Li–Cu–CNF electrolyte, and NMC811 or LiMn<sub>2</sub>O<sub>4</sub> cathodes, without any liquid electrolyte (Extended Data Fig. 10). By contrast, widely studied PEO-based SPEs can barely function with high-voltage cathodes<sup>33</sup>, showing the substantial advance offered by the room-temperature performance and high-voltage stability of Li–Cu–CNF.

## Conclusions

As a 1D solid-state ion conductor, Li–Cu–CNF demonstrates an exceptionally high ionic conductivity ( $1.5 \times 10^{-3} \text{ S cm}^{-1}$ ) and high Li<sup>+</sup>-transference number (0.78) at room temperature, which is made possible by decoupling the Li<sup>+</sup> transport from the local solvation environment. The Li<sup>+</sup> transport follows a rapid ion-hopping mechanism via the polar functional groups and bound water molecules available in the cellulose molecular channels that have been opened by Cu<sup>2+</sup>-coordination chemistry. The Li–Cu–CNF ion conductor, made with a simple and reproducible synthesis procedure, provides exceptional conductivity, electrochemical stability, processibility, transference number and mechanical strength for high-energy-density batteries (Fig. 4i). This 1D ion conductor can also function as an ionic building block for forming solid-state ionic conducting networks, enabling it to be compatible with thick cathodes and thus high-energy-density solid-state batteries. The success of this design strategy creates a class of polymer ion conductors that enable fast conduction by various cations (for example, Na<sup>+</sup>) with high room-temperature ionic conductivities that have so far been challenging for traditional polymer electrolytes (Supplementary Discussion 8, 9). For example, we investigated this same Cu<sup>2+</sup>-coordination approach for the synthesis of polymer ion conductors made of chitosan, alginate acid, carboxymethyl cellulose (CMC) and xanthan gum (XG) (Fig. 4j), all of which showed high room-temperature ionic conductivities ( $\sigma_{\text{Li}} = 3 \times 10^{-4} \text{ S cm}^{-1}$  for Li–Cu–chitosan;  $\sigma_{\text{Na}} = 2 \times 10^{-4} \text{ S cm}^{-1}$  for Na–Cu–alginate; and  $\sigma_{\text{Zn}} = 9 \times 10^{-4} \text{ S cm}^{-1}$  for Zn–Cu–XG/CNF). Our strategy provides both material and conceptual breakthroughs for the development of many other high-performance solid-state ion conductors that could have a broad impact beyond just safe solid-state batteries, examples of which could include electrochemical synaptic devices, solid-state sensors, and redox-controlled information processing and storage.

## Online content

Any methods, additional references, Nature Research reporting summaries, source data, extended data, supplementary information,

acknowledgements, peer review information; details of author contributions and competing interests; and statements of data and code availability are available at <https://doi.org/10.1038/s41586-021-03885-6>.

- Xu, K. Nonaqueous liquid electrolytes for lithium-based rechargeable batteries. *Chem. Rev.* **104**, 4303–4418 (2004).
- Long, L., Wang, S., Xiao, M. & Meng, Y. Polymer electrolytes for lithium polymer batteries. *J. Mater. Chem. A* **4**, 10038–10069 (2016).
- Gadjourova, Z., Andreev, Y. G., Tunstall, D. P. & Bruce, P. G. Ionic conductivity in crystalline polymer electrolytes. *Nature* **412**, 520–523 (2001).
- Croce, F., Appetecchi, G. B., Persi, L. & Scrosati, B. Nanocomposite polymer electrolytes for lithium batteries. *Nature* **394**, 456–458 (1998).
- Manthiram, A., Yu, X. & Wang, S. Lithium battery chemistries enabled by solid-state electrolytes. *Nat. Rev. Mater.* **2**, 16103 (2017).
- Lopez, J., Mackanic, D. G., Cui, Y. & Bao, Z. Designing polymers for advanced battery chemistries. *Nat. Rev. Mater.* **4**, 312–330 (2019).
- Zhao, W., Yi, J., He, P. & Zhou, H. Solid-state electrolytes for lithium-ion batteries: fundamentals, challenges and perspectives. *Electrochem. Energy Rev.* **2**, 574–605 (2019).
- Diederichsen, K. M., McShane, E. J. & McCloskey, B. D. Promising routes to a high Li<sup>+</sup> transference number electrolyte for lithium ion batteries. *ACS Energy Lett.* **2**, 2563–2575 (2017).
- Xue, Z., He, D. & Xie, X. Poly(ethylene oxide)-based electrolytes for lithium-ion batteries. *J. Mater. Chem. A* **3**, 19218–19253 (2015).
- Khurana, R., Schaefer, J. L., Archer, L. A. & Coates, G. W. Suppression of lithium dendrite growth using cross-linked polyethylene/poly(ethylene oxide) electrolytes: a new approach for practical lithium-metal polymer batteries. *J. Am. Chem. Soc.* **136**, 7395–7402 (2014).
- Mackanic, D. G. et al. Crosslinked poly(tetrahydrofuran) as a loosely coordinating polymer electrolyte. *Adv. Energy Mater.* **8**, 1800703 (2018).
- Pan, Q., Smith, D. M., Qi, H., Wang, S. & Li, C. Y. Hybrid electrolytes with controlled network structures for lithium metal batteries. *Adv. Mater.* **27**, 5995–6001 (2015).
- Bouchet, R. et al. Single-ion BAB triblock copolymers as highly efficient electrolytes for lithium-metal batteries. *Nat. Mater.* **12**, 452–457 (2013).
- Ma, Q. et al. Single lithium-ion conducting polymer electrolytes based on a super-delocalized polyanion. *Angew. Chem. Int. Edn* **55**, 2521–2525 (2016).
- Croce, F., Persi, L., Ronci, F. & Scrosati, B. Nanocomposite polymer electrolytes and their impact on the lithium battery technology. *Solid State Ion.* **135**, 47–52 (2000).
- Liu, W., Lin, D., Sun, J., Zhou, G. & Cui, Y. Improved lithium ionic conductivity in composite polymer electrolytes with oxide-ion conducting nanowires. *ACS Nano* **10**, 11407–11413 (2016).
- Wan, J. et al. Ultrathin, flexible, solid polymer composite electrolyte enabled with aligned nanoporous host for lithium batteries. *Nat. Nanotechnol.* **14**, 705–711 (2019).
- Xu, H. et al. High-performance all-solid-state batteries enabled by salt bonding to perovskite in poly(ethylene oxide). *Proc. Natl Acad. Sci. USA* **116**, 18815–18821 (2019).
- Lv, D. et al. Pure cellulose lithium-ion battery separator with tunable pore size and improved working stability by cellulose nanofibrils. *Carbohydr. Polym.* **251**, 116975 (2021).
- Zhao, D. et al. Cellulose-based flexible functional materials for emerging intelligent electronics. *Adv. Mater.* **33**, 2000619 (2020).
- Dahlström, C. et al. Ion conductivity through TEMPO-mediated oxidized and periodate oxidized cellulose membranes. *Carbohydr. Polym.* **233**, 115829 (2020).
- Zugenmaier, P. *Crystalline Cellulose and Derivatives* 1st edn (Springer-Verlag, 2008).
- Ogawa, Y. et al. Formation and stability of cellulose–copper–NaOH crystalline complex. *Cellulose* **21**, 999–1006 (2014).
- Alava, M. & Niskanen, K. The physics of paper. *Rep. Prog. Phys.* **69**, 669–723 (2006).
- Xie, J., Liang, Z. & Lu, Y.-C. Molecular crowding electrolytes for high-voltage aqueous batteries. *Nat. Mater.* **19**, 1006–1011 (2020).
- Kimura, K., Motomatsu, J. & Tominaga, Y. Correlation between solvation structure and ion-conductive behavior of concentrated poly(ethylene carbonate)-based electrolytes. *J. Phys. Chem. C* **120**, 12385–12391 (2016).
- Nair, J. R., Imholt, L., Brunklaus, G. & Winter, M. Lithium metal polymer electrolyte batteries: opportunities and challenges. *Electrochem. Soc. Interface* **28**, 55–61 (2019).
- Shi, S., Qi, Y., Li, H. & Hector, L. G. Defect thermodynamics and diffusion mechanisms in Li<sub>2</sub>CO<sub>3</sub> and implications for the solid electrolyte interphase in Li-ion batteries. *J. Phys. Chem. C* **117**, 8579–8593 (2013).
- Zheng, J., Tang, M. & Hu, Y.-Y. Lithium ion pathway within Li<sub>7</sub>La<sub>3</sub>Zr<sub>2</sub>O<sub>12</sub>/polyethylene oxide composite electrolytes. *Angew. Chem. Int. Edn* **55**, 12538–12542 (2016).
- He, X., Zhu, Y., Epstein, A. & Mo, Y. Statistical variances of diffusional properties from ab initio molecular dynamics simulations. *NPJ Comput. Mater.* **4**, 18 (2018).
- Kim, B., Lee, J. & Yu, I. Electrical properties of single-wall carbon nanotube and epoxy composites. *J. Appl. Phys.* **94**, 6724–6728 (2003).
- Zeng, X.-X. et al. Reshaping lithium plating/stripping behavior via bifunctional polymer electrolyte for room-temperature solid Li metal batteries. *J. Am. Chem. Soc.* **138**, 15825–15828 (2016).
- Qiu, J. et al. Enabling stable cycling of 4.2 V high-voltage all-solid-state batteries with PEO-based solid electrolyte. *Adv. Funct. Mater.* **30**, 1909392 (2020).

**Publisher's note** Springer Nature remains neutral with regard to jurisdictional claims in published maps and institutional affiliations.

© The Author(s), under exclusive licence to Springer Nature Limited 2021

## Methods

### Preparation of CNFs

CNFs were produced by (2,2,6,6-tetramethylpiperidin-1-yl)oxidanyl (TEMPO) oxidation of commercial bleached eucalyptus Kraft pulp (International Paper) and mechanical treatment in a microfluidizer (M-110EH Microfluidizer Processor) as before<sup>34</sup>. The resulting CNF suspension (roughly 1 wt% solid content) was stored at 4 °C for further treatment. CNF paper was fabricated by vacuum filtration of the CNF suspension. The filtrated CNF paper was placed between sheets of filter paper and pressed at room temperature for 24 h at a pressure of roughly 2 MPa to obtain dense CNF paper. To achieve aligned CNFs, wood slices (cut along the longitudinal direction, that is, the growth direction of the tree) were delignified by immersing and boiling in a NaClO<sub>2</sub> solution (5 wt%) with a pH of roughly 4.6 (adjusted by acetic acid) until the wood slices turned completely white (roughly 2 h). The delignified wood slices were then washed with deionized water three times to remove the residual chemicals and then hot-pressed at 60 °C for two days to obtain the aligned CNFs (that is, densified wood, different from the individual CNFs produced by TEMPO oxidation).

### Preparation of Cu<sup>2+</sup>-saturated alkaline solution

The Cu<sup>2+</sup>-saturated alkaline solution was made by immersing excess copper wire in NaOH solution (20 wt%), for example, 5 g of copper wire in 500 ml of NaOH solution. The solution was magnetically stirred until the NaOH solution turned blue after two to three days. Before use, this stock solution was stored with excess immersed copper wire. According to ICP analysis, the concentration of Cu<sup>2+</sup> in the Cu<sup>2+</sup>-saturated NaOH solution was 2.8 wt%.

### Preparation of Li–Cu–CNF

We fabricated Li–Cu–CNF through the following three steps. (1) CNFs (generally referring to any format of cellulose consisting of CNFs, including CNF suspension, cellulose paper or aligned CNFs) were immersed in Cu<sup>2+</sup>-saturated alkaline solution (20% NaOH) for one to two weeks until the CNFs gradually turned blue (reaching saturated Cu<sup>2+</sup> coordination with the CNFs), with the product referred to as Cu–CNF–NaOH. (2) The free water in the Cu–CNF–NaOH was then replaced by DMF solvent exchange, which was then evaporated to produce the Cu–CNF. (3) The Cu–CNF was soaked in a Li-salt solution (1 mol l<sup>-1</sup> LiPF<sub>6</sub> dissolved in ethylene carbonate/dimethyl carbonate (EC/DMC); 1:1 volumetric ratio) for two days in an argon-filled glovebox, followed by repeatedly pressing and wiping the absorbed liquid and evaporating the solvent in vacuum to obtain the Li–Cu–CNF solid-state ion conductor. For the Li–CNF control sample, the CNFs were treated using the same steps, except that the material was immersed in the NaOH solution without Cu<sup>2+</sup> in step 1.

For different uses of Li–Cu–CNF, the materials or synthesis process described above was slightly changed. To obtain Li–Cu–CNF with aligned orientation for measuring the intrinsic conductivity, mechanical strength and fibre XRD along the fibre direction, the aligned CNFs (produced from wood as above) were used as the CNF source in step 1 to produce the aligned Li–Cu–CNF as above. To fabricate the Li–Cu–CNF paper electrolyte, the cellulose paper was used as the CNF source in step 1 and was treated as above.

### Preparation of other M–Cu–polymers

The Li–Cu–CNF system was extended to other M–Cu–polymer systems via slightly modified synthesis methods. Here, aqueous solutions of chitosan, sodium alginate and sodium CMC (all from Sigma Aldrich) were cast-dried and pressed into thin films. The XG (TCI) was mixed with the TEMPO-oxidized CNF material (XG/CNF; mass ratio 1:1) in solution, filtrated, and pressed into a thin film. The polymer films were coordinated with Cu<sup>2+</sup> to form Cu–polymer via a similar method in step 1. The Cu–chitosan was further similarly treated via steps 2 and 3 for Li<sup>+</sup>

insertion. The Cu–CMC was soaked in a Na<sup>+</sup>-ion electrolyte (3 mol l<sup>-1</sup> NaClO<sub>4</sub> in DMF) for inserting Na<sup>+</sup> and forming Na–Cu–CMC. The Cu–alginate was treated with a Na<sup>+</sup>-ion electrolyte (4 mol l<sup>-1</sup> NaClO<sub>4</sub> aqueous solution) to form Na–Cu–alginate for Na<sup>+</sup> conduction. The Cu–XG/CNF was treated with a Zn<sup>2+</sup> electrolyte (2 mol l<sup>-1</sup> ZnSO<sub>4</sub> aqueous solution) to form Zn–Cu–XG/CNF for Zn<sup>2+</sup> conduction. All samples were dried in vacuum before electrochemical testing.

### Preparation of solid-state cathodes

To prepare the LiFePO<sub>4</sub> (BTR New Material Group) cathode mixed with Li–Cu–CNF, the Cu–CNF–NaOH suspension obtained in step 1 was washed and mixed with the cathode material and CNT (Carbon Solutions) (typical mass ratio of LiFePO<sub>4</sub>:CNT:Cu–CNF = 9:1:1) in water solution using a vortex mixer for 5 min, followed by ultrasonication for 30 s (FS110D, Fisher Scientific). The mixture was then either filtrated as a free-standing thick cathode or cast on aluminium foil with the addition of 9 wt% sodium alginate binder, followed by the same treatment as in steps 2 and 3. To measure the ion-percolation behaviour of Li–Cu–CNF in the cathode, the LiFePO<sub>4</sub> cathode was fabricated through the same filtration method using different ratios of Li–Cu–CNF (Li–CNF was used as the ‘zero’ Li–Cu–CNF control) and without CNTs. The solid-state NMC811 and LiMn<sub>2</sub>O<sub>4</sub> cathodes were made by casting the cathode materials with carbon black and poly(vinylidene fluoride) (dissolved in *N*-methyl-2-pyrrolidone) with a mass ratio of 8:1:1 on aluminium foil, followed by drying at 100 °C.

### Assembly of solid-state batteries

The solid-state batteries were assembled in an argon-filled glovebox. The Li symmetric cells were assembled by sandwiching the Li–Cu–CNF paper electrolyte between two Li metals. The solid-state full cells were made with a Li-metal anode, the Li–Cu–CNF electrolyte, and a cathode (LiFePO<sub>4</sub>, NMC811 or LiMn<sub>2</sub>O<sub>4</sub> cathodes made as described above). The solid-state flexible cell was assembled using a thin Li-metal anode, Li–Cu–CNF paper electrolyte, and LiFePO<sub>4</sub> cathode in a paper pouch.

### Characterization

A Hitachi SU-70 field emission SEM coupled with an energy-dispersive X-ray (EDX) spectroscopy system was used for SEM and elemental analysis. The fibre XRD measurements were conducted on a Xenocs Xeuss SAXS/WAXS system with a Cu K $\alpha$  ( $\lambda = 1.5418 \text{ \AA}$ ) source and Detris Pilatus 300k detector. A home-made sample holder was used to bring samples close to the detector. The content of Li and Cu in Li–Cu–CNF was analysed by dissolving the metal ions in the samples in nitric acid (5%) and measuring the metal concentration using a multi-collector ICP mass spectrometer (Thermo-Finnigan Element 2). FTIR was conducted on a Nexus 670 made by Thermo Electron with a ‘Smart Endurance’ attenuated total reflectance accessory. Stress–strain measurements of Li–Cu–CNF (along the cellulose fibre direction) were carried out using a Tinius Olsen H5KT testing machine.

XAS measurements were carried out at the 8-ID Beamline of the National Synchrotron Light Source II at Brookhaven National Laboratory (BNL). X-ray absorption near-edge spectroscopy (XANES) and extended X-ray absorption fine structure (EXAFS) data were collected at the Cu K-edge in transmission mode. The samples were placed between two Kapton tapes, which allow for high transmissivity for X-ray measurements. The spectra of the standards were obtained from copper foil (provided by BNL), commercial Cu<sub>2</sub>O powder and CuO powder (Sigma Aldrich). XAS data were analysed using the IFEFFIT package, which included ATHENA and ARTEMIS<sup>35</sup>.

QENS spectra were measured at the high-flux backscattering spectrometer (HFBS) in elastic scan mode. In this mode, only elastically scattered neutrons are counted, and a drop in the intensity indicates the presence of the motions in the dynamic range accessible by the instrument. The HFBS has an instrument resolution of about 0.8 eV, which is equivalent to about 2 ns. The data are simultaneously collected for



angular momentum transfer,  $Q$ , in the range  $0.25 \text{ \AA}^{-1}$  to  $1.75 \text{ \AA}^{-1}$ . In this analysis, the entire  $Q$  range was used. All samples were loaded in the standard aluminium sample holders and sealed with indium. All samples were loaded at 296 K and cooled to 4 K at a ramp rate of  $0.8 \text{ K min}^{-1}$ , followed by heating back to 296 K at the same ramp rate. The measured elastic intensity can be used to calculate the mean square displacement (MSD) of the sample using a classic Gaussian approximation:

$$\frac{I(T)}{I(T_{\min})} = \exp\left(-\frac{Q^2 \langle u^2 \rangle}{3}\right) \quad (1)$$

where  $I(T)$  is the elastic intensity measured at temperature  $T$ ;  $I(T_{\min})$  is the intensity at the base temperature of 4 K; and  $\langle u^2 \rangle$  is the MSD.

To measure the content of water and EC, we conducted 1D  $^1\text{H}$  MAS NMR analysis of Li–Cu–CNF, using a dry Cu–CNF sample as a control (without EC and dried at  $30 \text{ }^\circ\text{C}$  under vacuum for three days to remove water), on a 300 MHz Varian NMR spectrometer with a 1.6-mm double-resonance-probe head (spun at 33 kHz MAS). The  $^1\text{H}$  chemical shifts were externally referenced to TMS.

$^7\text{Li}$  and  $^{19}\text{F}$  PFG NMR were conducted on a 300 MHz NMR spectrometer on a double-resonance probe equipped with a maximum gradient of  $1,200 \text{ G cm}^{-1}$ . Double-stimulated echo or spin-echo pulse sequences were used to measure the diffusion coefficients. The signal was accumulated by using a minimum of 64, up to a maximum of 1,536, transients with a 2-s recycling delay. The gradient strength was varied from  $2\text{--}50 \text{ G cm}^{-1}$  or  $2\text{--}700 \text{ G cm}^{-1}$  over 16 increments. The diffusion time ( $\Delta$ ) and the diffusion pulse length ( $\delta$ ) were in the range of 50–400 ms and 2–9 ms, respectively. The diffusion coefficients ( $D$ ) were calculated using the Stejskal–Tanner equation:

$$\frac{I}{I_0} = \exp\left[-(G\gamma\delta)^2\left(\Delta - \frac{\delta}{3}\right)D\right] \quad (2)$$

in which  $\gamma$  is the gyromagnetic ratio and  $G$  is the gradient strength.

For isotope tracing, the tracer exchange ( $^6\text{Li} \rightarrow ^7\text{Li}$ ) was driven by electrochemical cycling using  $^6\text{Li}$ -enriched metal (95 atom%; Sigma Aldrich) as electrode foils. The Li–Cu–CNF (or Li–CNF as a control) electrolyte was assembled between two  $^6\text{Li}$  foils to form a symmetric cell ( $^6\text{Li}/\text{Li–Cu–CNF}/^6\text{Li}$ ). The cell was galvanically polarized for 50 cycles with a current density of  $32 \mu\text{A cm}^{-2}$ , and the current switched the direction every 30 min. After cycling, the electrolyte was removed from the cell for  $^6\text{Li}$  NMR measurements.  $^6\text{Li}$  magic-angle-spinning NMR experiments were performed on a Bruker Avance III-500 spectrometer with a  $^6\text{Li}$  Larmor frequency of 73.6 MHz. Samples were packed in 2.5-mm rotors and spun at a speed of 25 kHz. We used a single pulse to acquire the  $^6\text{Li}$  NMR spectra with a  $90^\circ$  pulse length of 2.5  $\mu\text{s}$  and a recycle delay of 10 s.  $^6\text{Li}$  NMR chemical shifts were referenced to solid LiCl at  $-1.1$  ppm. We fitted the  $^6\text{Li}$  NMR spectra (Extended Data Fig. 6) using Gaussian–Lorentzian functions<sup>29</sup>. The fitted peaks were assigned to different chemical environments of  $\text{Li}^+$  on the basis of experiments (reference NMR spectra in Extended Data Fig. 6c, d) or literature references<sup>36,37</sup>. The peak areal integrals were normalized on the basis of the mass of the samples and the number of signal averages.

### Electrochemical tests

Electrochemical tests (electrochemical impedance spectroscopy (EIS), d.c. polarization and LSV) were done on a Biologic electrochemical working station. EIS spectra were measured in a frequency range of 1 MHz to 1 Hz with a voltage amplitude of 20 mV. We used two Li//Li–Cu–CNF//SS cells to conduct separate cathodic (from OCV to 5.4 V) and anodic (from OCV to 0 V) scans at  $0.1 \text{ mV s}^{-1}$  to measure the electrochemical stability window of Li–Cu–CNF. Electrochemical stripping/plating for Li symmetric cells and galvanostatic cycling tests for solid-state full cells were conducted on a LAND electrochemical testing system with galvanostatic conditions.

For ionic conductivity tests, we first confirmed the  $\text{Li}^+$  transport along the fibre direction of the Li–Cu–CNF ion conductor through the galvanostatic Li plating/stripping cycling (Extended Data Fig. 5a) between two ends of the aligned Li–Cu–CNF (length 1 cm) at room temperature. To distinguish the resistances of the electrolyte and Li–electrolyte interface, we measured the EIS of the same aligned Li–Cu–CNF at different lengths (Extended Data Fig. 5b). The EIS spectra of the Li–Cu–CNF ion conductor show two semi-circles, which are attributed to the electrolyte and interface resistance. The semi-circle at the high-frequency region increases linearly as we increase the electrolyte length from 1 cm to 3 cm (Extended Data Fig. 5c). Thus, the high-frequency semi-circle is attributed to the resistance of the Li–Cu–CNF electrolyte. The calculated  $\text{Li}^+$  conductivity of Li–Cu–CNF at different temperatures (Extended Data Fig. 5d) is plotted in Fig. 3b, following an Arrhenius-type relationship.

We then tested the EIS of a Li–Cu–CNF paper electrolyte made up of randomly oriented fibres (sandwiched between two stainless-steel spacers) at different temperatures ( $60 \text{ }^\circ\text{C}$  to  $-20 \text{ }^\circ\text{C}$ ; Extended Data Fig. 5e, f) to obtain the temperature-dependent through-plane ionic conductivity of the Li–Cu–CNF paper electrolyte (Extended Data Fig. 5g). The Li–Cu–CNF electrolyte shows a through-plane ionic conductivity of  $3.4 \times 10^{-4} \text{ S cm}^{-1}$  at room temperature and an Arrhenius-type temperature-dependent ionic conductivity ( $60 \text{ }^\circ\text{C}$  to  $-20 \text{ }^\circ\text{C}$ ) without an abrupt conductivity drop below  $0 \text{ }^\circ\text{C}$ . We attribute this lack of transition to the  $\text{H}_2\text{O}$  molecules in the material being bound rather than free, and therefore lacking a freezing point<sup>38</sup>.

We used d.c. polarization (Extended Data Fig. 5h) to measure the  $\text{Cu}^{2+}$  diffusion using a Cu//Cu–CNF//Cu cell, which allows only  $\text{Cu}^{2+}$  transport without  $\text{Li}^+$  conduction. Therefore, the  $\text{Cu}^{2+}$  in Li–Cu–CNF is considered immobile and the ionic conductivity of Li–Cu–CNF is contributed by the material's  $\text{Li}^+$  rather than  $\text{Cu}^{2+}$ .

We measured the  $\text{Li}^+$ -transference numbers ( $t_{\text{Li}}$ ) in Li–Cu–CNF and Li–CNF (without Cu coordination) using the Bruce–Vincent method<sup>39</sup>. d.c. polarization measurements were conducted with a potential of  $\Delta V = 10 \text{ mV}$  in the Li//Li–Cu–CNF//Li and Li//Li–CNF//Li cells until the current reached a steady state, and corresponding EIS measurements were collected before and after the d.c. polarization (Extended Data Fig. 5i–l).  $t_{\text{Li}}$  was calculated according to:

$$t_{\text{Li}} = \frac{I_{\text{ss}}(\Delta V - I_0 R_0)}{I_0(\Delta V - I_{\text{ss}} R_{\text{ss}})} \quad (3)$$

where  $\Delta V$  is the applied potential,  $I_0$  is the initial current,  $R_0$  is the initial resistance,  $I_{\text{ss}}$  is the steady-state current, and  $R_{\text{ss}}$  is the steady-state resistance. The measured results of these parameters are listed in Extended Data Fig. 5m.

### Density functional theory (DFT) calculations

To predict the oxidation/reduction voltage and binding energies, we carried out DFT calculations using the Gaussian 16 code (revision AVX2)<sup>40</sup>. We used the hybrid PBE0 functional<sup>41</sup> and the basis set 6-311+G\*\* for geometry optimizations, energy calculations and frequency calculations. We adopted the D3 version of Grimme's dispersion with Becke–Johnson damping (GD3BJ)<sup>42</sup> in order to correct for weak interactions.

### Molecular dynamics simulations

The crystalline Cu–CNF–NaOH was built using the Materials Studio (MS, version 7.0)<sup>43</sup> Visualizer with experimental input for the lattice constant and crystal symmetry<sup>23</sup>. The Forcite module in MS was used to conduct classical molecular dynamics (MD) simulations. The COMPASS II force-field<sup>44</sup>, which is extended for polymer systems, was adopted to account for both the bonded and the non-bonded interactions. The force-field type and charges listed in Extended Data Fig. 2a result in Li–O interactions for different functional groups comparing well with DFT calculations (Extended Data Fig. 2b). As the  $\text{Cu}^{2+}$  did not diffuse in experiments, an additional Harmonic potential with a force constant of  $25,000 \text{ kcal mol}^{-1} \text{ \AA}^{-2}$

was applied to the Cu–O bond term to keep the Cu–O distances at the values obtained from DFT calculations (Extended Data Fig. 2c). The Ewald summation method was used to calculate the Coulombic interactions with an accuracy of  $0.001 \text{ kcal mol}^{-1}$  and a cutoff distance of  $12.5 \text{ \AA}$ . The Nosé method<sup>45</sup> was used for constant temperature dynamics and the Berendsen method<sup>46</sup> was used for NPT (constant particle number, pressure and temperature) dynamics. A total simulation time of  $5.0 \text{ ns}$  with a timestep of  $1.0 \text{ fs}$  was applied to typical production MD runs.

### Computational models and procedure

We started by building the atomic structure of the crystalline Cu–CNF–NaOH on the basis of the experimental inputs on the lattice parameters and crystal symmetry. The  $2 \times 2$  supercell of the Cu–CNF backbone structure (Extended Data Fig. 2d) was assigned with lattice parameters of  $a = b = 15.0 \text{ \AA}$  with a hexagonal symmetry, which agrees with the experimental measurements. Every two nearby cellulose chains were connected by one Cu atom through the hydroxyl O atoms in the simulation cell. A long cell was built with  $c = 90.0 \text{ \AA}$ . In our MD simulations, the  $2 \times 2$  supercell was used to avoid the interactions between periodic images. An appropriate number of  $\text{H}_2\text{O}$  molecules were added by the Amorphous Cell module in MS (Extended Data Fig. 2e). Our simulated cell contained 144 AGUs, 1,600 water molecules and 12 Cu atoms. Twenty-four  $\text{CH}_2\text{OH}$  groups were replaced by COOH groups. Room temperature ( $298 \text{ K}$ ) and a pressure of  $1 \text{ bar}$  were kept constant during NPT dynamics for  $1.0 \text{ ns}$  to obtain the density at this stage. Next, we removed most water molecules to model the drying process with only 144  $\text{H}_2\text{O}$  molecules left in the system. Although this is the structure used for most analysis (unless noted otherwise), additional systems with 96, 48 and 0  $\text{H}_2\text{O}$  molecules ( $\text{H}_2\text{O}:\text{AGU} = 2:3, 1:3$  and 0, respectively) were simulated to evaluate the effect of bound water concentration (Extended Data Fig. 7d).  $\text{Li}^+$  insertion was achieved by replacing the 24 –COOH groups with 24 –COOLi groups, and the 24 – $\text{CH}_2\text{OH}$  groups with 24 – $\text{CH}_2\text{OLi}$  groups (Extended Data Fig. 2g). There were 48  $\text{Li}^+$  ions in the modelling system, and the Li:AGU ratio was set to 1:3, which is the value estimated in the ICP experiment. Then NPT dynamics simulations were performed to obtain the equilibrated amorphous Cu–CNF (Extended Data Fig. 2f) and Li–Cu–CNF (Extended Data Fig. 2g). A high temperature of  $600 \text{ K}$  was used to accelerate the dynamics; compared with room-temperature simulations, no change in mechanism was observed owing to the use of classical force field. Finally, production runs for  $5.0 \text{ ns}$  were carried out at  $600 \text{ K}$  under an NVT (constant particle number, volume and temperature) ensemble to investigate the Li-transport mechanism. Li–Cu–CNF without any  $\text{H}_2\text{O}$  molecules was also simulated for comparison. Additional MD simulations on Li–Cu–CNF systems with EC and  $\text{LiPF}_6$  included were also conducted to investigate the effects of residual EC and  $\text{PF}_6^-$  and to calculate the transference number (see Supplementary Discussions 2, 10).

### XANES calculations

Cu K-edge theoretical XANES calculations for the  $\text{Cu}-(\text{AGU})_2$  system (Extended Data Fig. 2c) were conducted in the framework of the real-space full multiple scattering scheme with the muffin-tin approximation for the potential as implemented in the FDMNES code<sup>47</sup>.

### Data availability

The data that support the findings of this study are available within this article and its Supplementary Information. Additional data are available from the corresponding authors upon reasonable request. Source data are provided with this paper.

- Saito, T., Kimura, S., Nishiyama, Y. & Isogai, A. Cellulose nanofibers prepared by TEMPO-mediated oxidation of native cellulose. *Biomacromolecules* **8**, 2485–2491 (2007).
- Ravel, B. & Newville, M. ATHENA, ARTEMIS, HEPHAESTUS: data analysis for X-ray absorption spectroscopy using IFEFFIT. *J. Synchrotron Radiat.* **12**, 537–541 (2005).
- Wan, C. et al. Multinuclear NMR study of the solid electrolyte interface formed in lithium metal batteries. *ACS Appl. Mater. Interfaces* **9**, 14741–14748 (2017).
- Zou, J., He, H., Dong, J. & Long, Y. A guest/host material of  $\text{LiCl}/\text{H-STI}$  (stilbite) zeolite assembly: preparation, characterization and humidity-sensitive properties. *J. Mater. Chem.* **14**, 2405–2411 (2004).
- Zhou, X., Zhao, F., Guo, Y., Rosenberger, B. & Yu, G. Architecting highly hydratable polymer networks to tune the water state for solar water purification. *Sci. Adv.* **5**, eaaw5484 (2019).
- Evans, J., Vincent, C. A. & Bruce, P. G. Electrochemical measurement of transference numbers in polymer electrolytes. *Polymer* **28**, 2324–2328 (1987).
- Frisch, M. J. et al. Gaussian 16 Rev. AVX2 (Gaussian Inc., Wallingford, CT, 2016).
- Adamo, C. & Barone, V. Toward reliable density functional methods without adjustable parameters: The PBE0 model. *J. Chem. Phys.* **110**, 6158–6170 (1999).
- Grimme, S., Ehrlich, S. & Goerigk, L. Effect of the damping function in dispersion corrected density functional theory. *J. Comput. Chem.* **32**, 1456–1465 (2011).
- BIOVIA. Materials Studio 7.0 (Dassault Systèmes, San Diego, CA, 2013).
- Sun, H. et al. COMPASS II: extended coverage for polymer and drug-like molecule databases. *J. Mol. Model.* **22**, 47 (2016).
- Nosé, S. A molecular dynamics method for simulations in the canonical ensemble. *Mol. Phys.* **52**, 255–268 (1984).
- Berendsen, H. J. C., Postma, J. P. M., Gunsteren, W. F. V., DiNola, A. & Haak, J. R. Molecular dynamics with coupling to an external bath. *J. Chem. Phys.* **81**, 3684–3690 (1984).
- Joly, Y. X-ray absorption near-edge structure calculations beyond the muffin-tin approximation. *Phys. Rev. B Condens. Matter Mater. Phys.* **63**, 125120 (2001).
- Persson, I. et al. EXAFS study on the coordination chemistry of the solvated copper(II) ion in a series of oxygen donor solvents. *Inorg. Chem.* **59**, 9538–9550 (2020).
- Schmidt, D. A. & Miki, K. Structural correlations in liquid water: a new interpretation of IR spectroscopy. *J. Phys. Chem. A* **111**, 10119–10122 (2007).
- Wallace, V. M., Dhuma, N. R., Zehentbauer, F. M., Kim, H. J. & Kiefer, J. Revisiting the aqueous solutions of dimethyl sulfoxide by spectroscopy in the mid- and near-infrared: experiments and Car–Parrinello simulations. *J. Phys. Chem. B* **119**, 14780–14789 (2015).
- Torres, J. et al. A neutron scattering and electron microscopy study of the structure, wetting, and freezing behavior of water near hydrophilic  $\text{CuO}$ -nanostructured surfaces. *J. Appl. Phys.* **125**, 025302 (2019).

**Acknowledgements** L.H. and C.Y. acknowledge support from the University of Maryland A. James Clark School of Engineering. Q.W. and Y.Q. acknowledge support from the National Science Foundation (NSF) under grant DMR-2054438. Y.-Y.H. acknowledges support from the NSF under grant DMR-1847038. Solid-state NMR experiments were carried out at the National High Magnetic Field Laboratory, which is supported by the NSF through NSF/DMR-1644779 and the State of Florida. The NMR diffusion work at Hunter College was supported in part by the US Office of Naval Research, grant N00014-20-1-2186. This research used resources at the 8-ID Beamline of the National Synchrotron Light Source II, a US Department of Energy Office of Science User Facility operated by Brookhaven National Laboratory under contract no. DE-SC0012704. Access to the High Flux Backscattering Spectrometer was provided by the Center for High Resolution Neutron Scattering, a partnership between the National Institute of Standards and Technology (NIST) and the NSF under agreement DMR-1508249. Certain commercial equipment, instruments and materials are identified in this paper in order to specify the experimental procedure adequately. Such identification is not intended to imply recommendation or endorsement by the NIST. K.X. acknowledges support from the Joint Centre for Energy Security Research (JCESR), an energy hub funded by the US Department of Energy, Office of Science, Basic Energy Science under IAA SN2020957. We thank F. Lin, D. Hou and Z. Yang from Virginia Tech for providing the NMC811 cathode material.

**Author contributions** L.H. conceived the SPE concept and supervised the project. C.Y. and W.X. designed the experiments and conducted the material synthesis, characterization and electrochemical tests. S.H. and Y.G. also contributed to the material synthesis. Y.Q. and Q.W. carried out the DFT and MD simulations and XANES calculation. X.Z. and R.B. contributed to the structural analysis. M.N.G. and S.G. carried out the NMR analysis and determination of the ion diffusion coefficient. J.Z., P.W. and Y.-Y.H. carried out the  $^6\text{Li}$  NMR analysis. Y.M. and M.T. carried out the neutron-scattering characterization. B.H.K. and F.J. contributed to the XAS experiment. C.W. provided  $\text{LiMn}_2\text{O}_4$  material and assisted with testing and evaluating the electrochemical stability window. L.H., C.Y., Q.W., A.B., C.W., A.I., P.A., K.X. and M.W. drafted the paper. All authors contributed to the final manuscript.

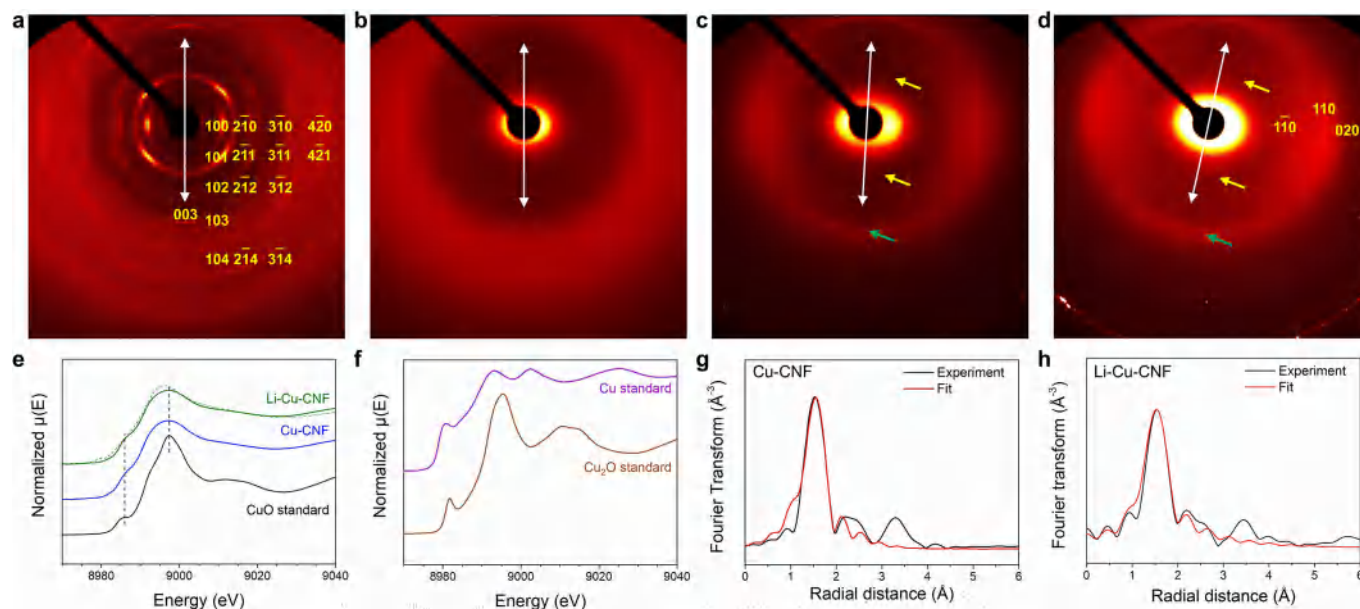
**Competing interests** The authors declare no competing interests.

### Additional information

**Supplementary information** The online version contains supplementary material available at <https://doi.org/10.1038/s41586-021-03885-6>.

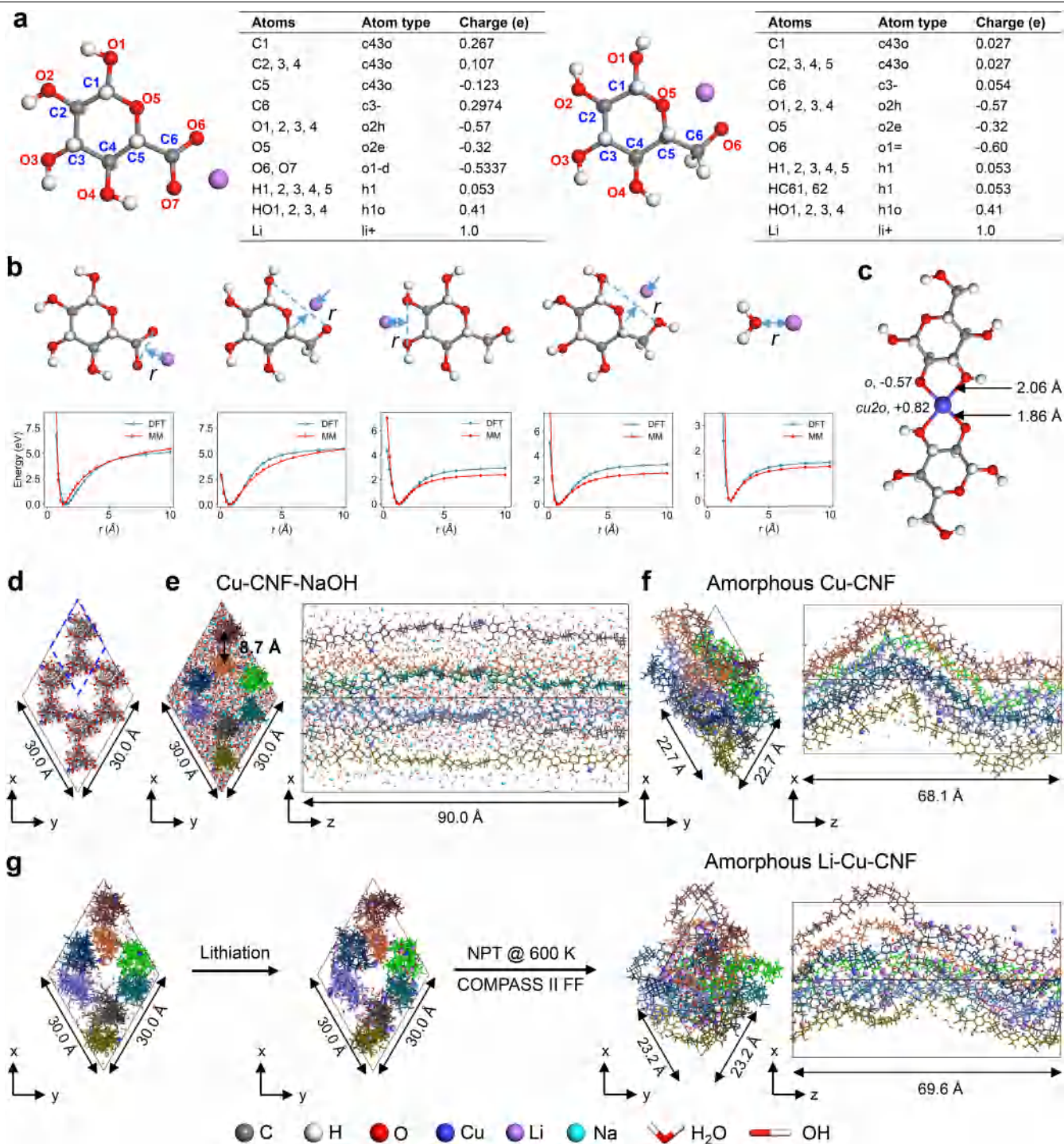
**Correspondence and requests for materials** should be addressed to Yue Qi or Liangbing Hu. **Peer review information** Nature thanks Lynden Archer and the other, anonymous, reviewer(s) for their contribution to the peer review of this work.

**Reprints and permissions information** is available at <http://www.nature.com/reprints>.



**Extended Data Fig. 1 | Structural characterization during the synthesis of Li-Cu-CNF.** **a-d**, Fibre XRD patterns of the CNFs (in the format of densified wood for high-resolution diffraction patterns) after the following treatment steps. **a**, Cu-CNF-NaOH obtained from  $\text{Cu}^{2+}$ -saturated NaOH aqueous solution. Peaks are indexed on the basis of the literature<sup>23</sup>. The (003) reflection is observed with a spacing of 0.51 nm, while the (001) and (002) reflections are absent, indicating that the Cu-CNF-NaOH features a threefold symmetric structure along the direction of the cellulose molecular chain. **b**, Cu-CNF washed with water to remove NaOH, demonstrating an amorphous structure. **c**, Cu-CNF after removing water by DMF exchange and evaporating DMF. The fibre XRD pattern shows a mostly amorphous structure with a small angle peak at roughly 2 nm corresponding to cellulose II<sup>22</sup>, possibly because of a small number of cellulose chains without coordinated Cu that form cellulose II after NaOH is removed. A high  $q$  peak at roughly 0.4 nm in the equatorial direction indicates the average molecular chain-to-chain distance of cellulose II. The green arrow in the meridian direction shows a peak corresponding to 0.47 nm in real space. The yellow arrows are pointing to peaks indicating the repeating unit of the Cu-CNF is roughly 1 nm along the cellulose chain. The 0.47 nm and

1 nm repeating distances are absent in all known cellulose structures, and therefore we attribute them to the unique structure of the Cu-CNF. **d**, Li-Cu-CNF after inserting  $\text{Li}^+$  in Cu-CNF and evaporating the solvent. The amorphous cellulose structure is maintained with some weak diffraction peaks of cellulose II. The yellow and green arrows indicate the same peaks as in **c**. **e-h**, XAS analysis of the Cu-CNF and Li-Cu-CNF samples. **e, f**, Cu K-edge X-ray absorption near edge structure (XANES) spectra of: **e**, Cu-CNF, Li-Cu-CNF and a CuO standard; **f**,  $\text{Cu}_2\text{O}$  and Cu standard samples. The green dashed line shows the calculated XANES spectrum of Li-Cu-CNF, in good agreement with the experimentally measured spectrum. Cu-CNF and Li-Cu-CNF show similar yet broadened pre-edge peaks to CuO at 8,986 eV ( $1s \rightarrow 3d$  transition), without the characteristic peaks of  $\text{Cu}_2\text{O}$  or Cu metal, indicating that the Cu ions in Cu-CNF and Li-Cu-CNF are of +2 valency. **g, h**, Fourier-transformed Cu K-edge extended X-ray absorption fine structure (EXAFS) spectra of: **g**, Cu-CNF; **h**, Li-Cu-CNF. On the basis of the EXAFS spectra, in Cu-CNF and Li-Cu-CNF, the  $\text{Cu}^{2+}$  are bonded with O atoms with an average bonding distance of 1.97 Å, consistent with that in reported Cu-organic complexes<sup>48</sup>, indicating that the  $\text{Cu}^{2+}$  is coordinated with the hydroxyl groups of the cellulose molecules.

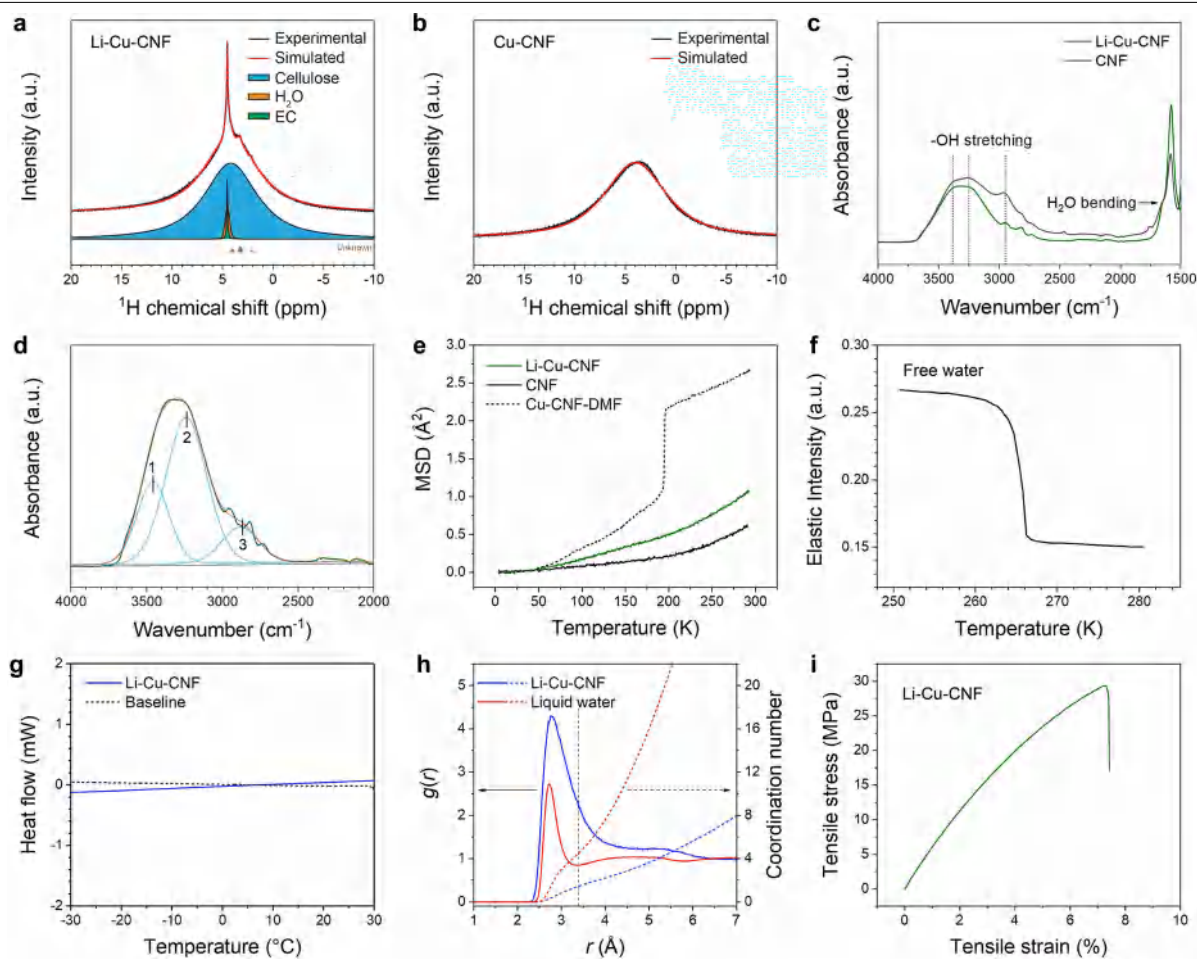


Extended Data Fig. 2 | See next page for caption.



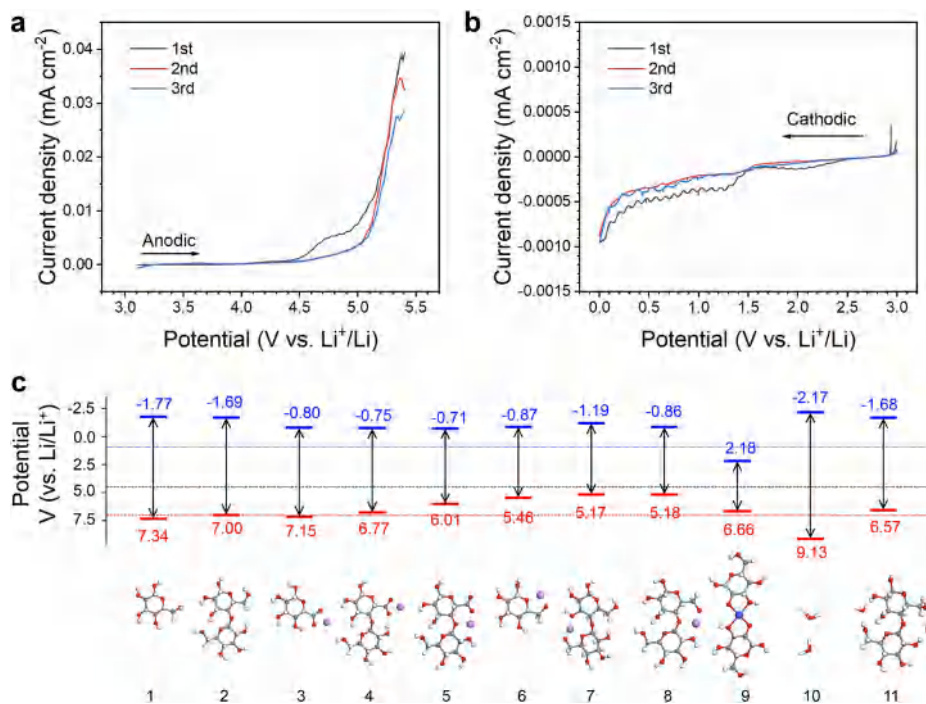
**Extended Data Fig. 2 | DFT calculations and MD simulations of the Li–Cu–CNF structure.** **a**, Assigned COMPASS II force-field types and atomic charges in typical cellulose units for MD simulations. **b**, Optimized atomic structures of the representative systems of Li–Cu–CNF used to evaluate interactions between  $\text{Li}^+$  and different oxygen-containing functional groups and water molecules, and corresponding energy–distance relationships for different  $\text{Li}^+$ -bonding environments given by molecular mechanics calculations using COMPASS II FF and DFT calculations. The difference between the total system energy at  $r=10.0 \text{ \AA}$  and the minimum energy is taken as the  $\text{Li}^+$ -dissociation energy. The  $\text{Li}^+$  is strongly bonded with both anionic  $\text{COO}^-$  and  $\text{RO}^-$  groups with dissociation energies of more than 5.0 eV. The dissociation energy of the  $\text{Li}^+$  is roughly 3.0 eV for ROH and EO groups, and 1.5 eV for  $\text{H}_2\text{O}$  molecules. The strong interactions between the  $\text{Li}^+$  and one or two oxygen species in cellulose suggest slow  $\text{Li}^+$  movements in the absence of multiple Li–O coordination. In the  $\text{H}_2\text{O}$  molecule, the O atom has an atom type of *o2\** and charge of  $-0.82 e$ , while the H atom has an atom type of *h1o* and a charge of  $+0.41 e$  for force-field calculations. **c**, To simulate  $\text{Cu}^{2+}$  coordination in cellulose, we optimized the atomic structure of two AGUs connected by one  $\text{Cu}^{2+}$  ( $\text{Cu}-(\text{AGU})_2$  system) to serve as a structural building block. Two H atoms are deprotonated by the Cu. The

average optimized Cu–O bond length ( $1.96 \text{ \AA}$ ) is close to that observed in the experiment ( $1.97 \text{ \AA}$ ), and the calculated XANES of the  $\text{Cu}-(\text{AGU})_2$  system is also in good agreement with the experimental measurement (Extended Data Fig. 1e), showing that our computational model for the structure of the Cu–O complex is reasonable. Atom types and atomic charges in force-field calculations are given for Cu and its connected O atoms, which are categorized as ROH for statistics (Fig. 3d in the main text). **d**, Top view of a  $2 \times 2$  supercell of the periodic Cu-coordinated CNF structure as a starting structure for the simulation, built with the most reasonable model that we proposed on the basis of the fibre XRD pattern (Fig. 2c). Every two nearby cellulose chains are connected by one Cu atom through the hydroxyl oxygen atoms. The unit cell is denoted by dashed blue lines. **e**, Top and side views of the Cu–CNF–NaOH. **f**, Top and side views of the amorphous Cu–CNF obtained by removing NaOH aqueous solution from Cu–CNF–NaOH and then equilibrating the system with NPT dynamics simulations. In Cu–CNF, we reserved 144  $\text{H}_2\text{O}$  molecules to keep an  $\text{H}_2\text{O}:\text{AGU}$  ratio of 1:1. **g**, Schematic of the computational approach used to obtain the atomic structure of the final amorphous Li–Cu–CNF model (top and side views).



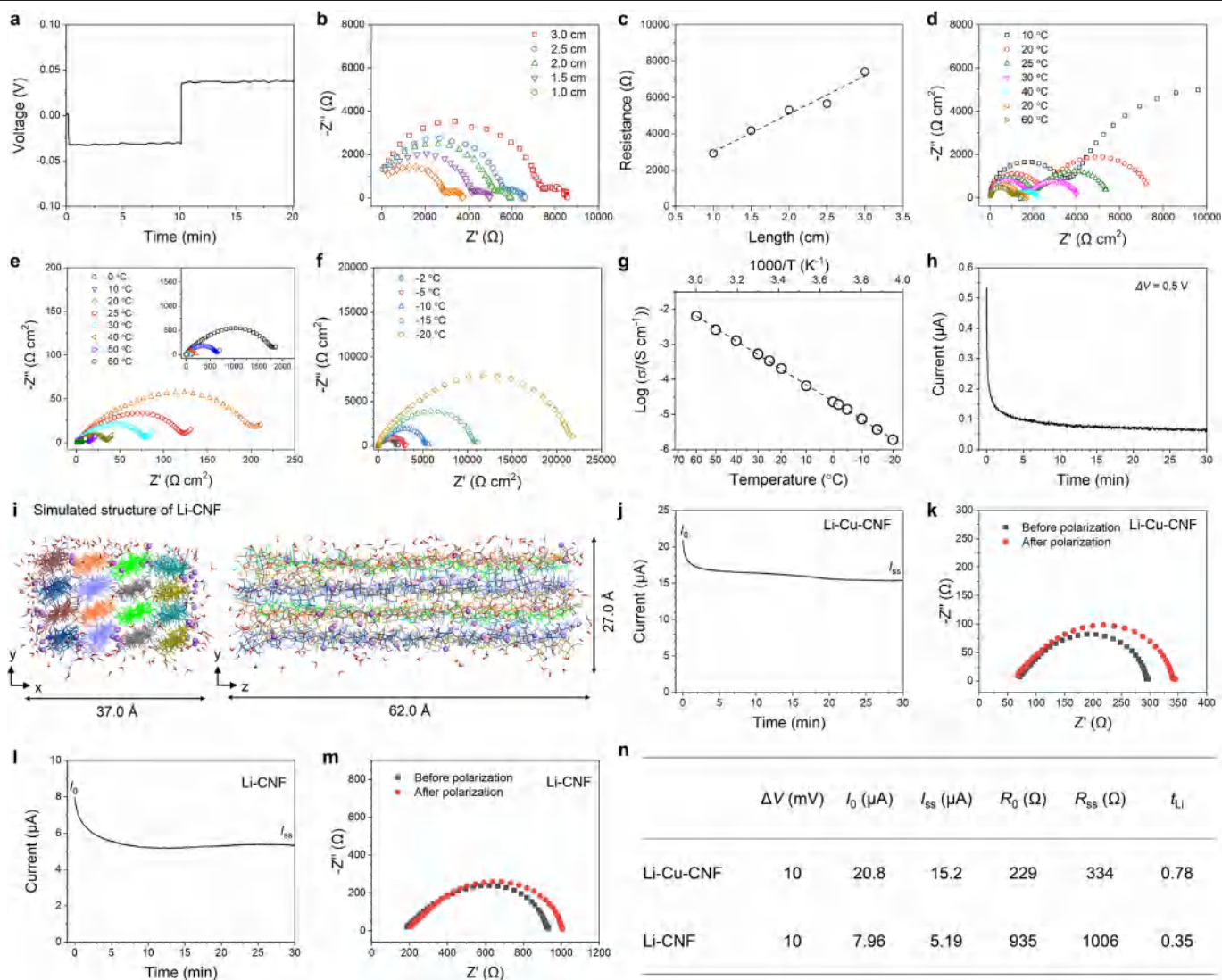
**Extended Data Fig. 3 | Bound water analysis of Li-Cu-CNF.** **a**,  $^1\text{H}$  MAS NMR spectra of Li-Cu-CNF with peak deconvolution. **b**,  $^1\text{H}$  MAS NMR spectra of Cu-CNF (dried at  $30^\circ\text{C}$  under vacuum for three days to remove water). **c**, FTIR of the pristine CNFs and solid-state Li-Cu-CNF. Both the pristine CNFs and Li-Cu-CNF show a broad -OH stretching peak at roughly  $3,300\text{ cm}^{-1}$ . **d**, The -OH stretching peak of Li-Cu-CNF deconvoluted into three bands at  $3,464\text{ cm}^{-1}$ ,  $3,235\text{ cm}^{-1}$  and  $2,886\text{ cm}^{-1}$ , which can be assigned to bound water molecules in different hydrogen-bonding states<sup>49,50</sup>. **e**, The atomic mean square displacement (MSD) change in CNF and Li-Cu-CNF as a function of temperature, as measured by QENS. The Cu-CNF sample after DMF solvent exchange with some residual DMF (Cu-CNF-DMF) is also shown for

comparison. **f**, Elastic neutron-scattering intensity of free water plotted against temperature ( $60\ \mu\text{l H}_2\text{O}$  on Cu foil) upon cooling; data derived from ref.<sup>51</sup>. **g**, DSC curve of Li-Cu-CNF in a cooling process from  $30^\circ\text{C}$  to  $-30^\circ\text{C}$ . **h**, Plots of  $\text{H}_2\text{O}$ - $\text{H}_2\text{O}$  radial distribution function (RDF) (solid lines) and coordination number (dashed lines) in liquid bulk water (red lines) and Li-Cu-CNF (blue lines). The first minimum of the RDF plot for the liquid bulk water system at  $3.4\ \text{\AA}$  (indicated by the black dashed line) was applied to calculate the coordination numbers. The distance is defined as the distance between the O atoms of the  $\text{H}_2\text{O}$  molecules. **i**, Stress-strain curve of Li-Cu-CNF along the direction of the CNF fibre. For more analysis, see Supplementary Discussion 11.



**Extended Data Fig. 4 | Electrochemical stability of Li-Cu-CNF.** **a, b**, The electrochemical stability window of Li-Cu-CNF was measured by both anodic and cathodic LSV scans at  $0.1 \text{ mV s}^{-1}$ . **a**, The first three anodic scans from OCV to 5.4 V. **b**, The first three cathodic scans from OCV to 0 V. **c**, Top, reduction and oxidation potentials (versus  $\text{Li}^+/\text{Li}$ ) obtained from DFT calculations for (bottom) different structures representative of the cellulose and Li-Cu-CNF systems, including: (1) glucose; (2) AGU dimer; (3) AGU-COOLi; (4, 5) two isomers of  $(\text{AGU})_2\text{-COOLi}$ ; (6) AGU- $\text{CH}_2\text{OLi}$ ; (7, 8) two isomers of

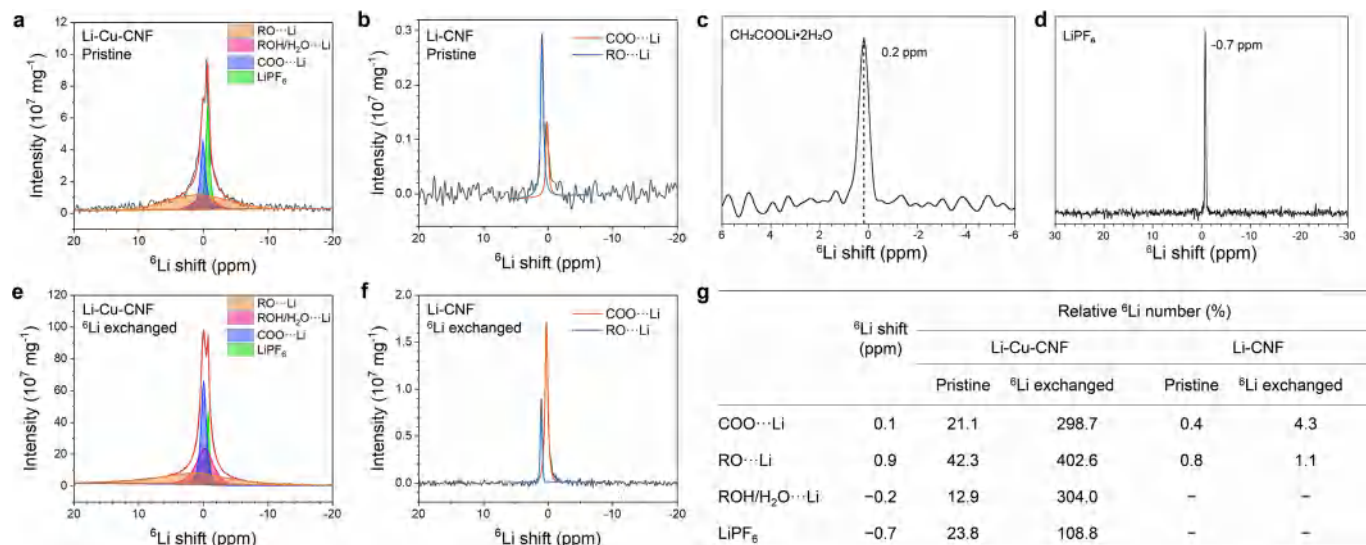
$(\text{AGU})_2\text{-CH}_2\text{OLi}$ ; (9) Cu- $(\text{AGU})_2$ ; (10)  $\text{H}_2\text{O}$  dimer; and (11)  $(\text{AGU})_2\text{-(H}_2\text{O)}_2$ . C, H, O, Li and Cu atoms are represented by grey, white, red, purple and blue spheres, respectively. Water molecules are depicted with stick models. The experimental oxidation potential for Li-Cu-CNF (black) and the redox potentials for EC are denoted with dashed lines (blue for reduction and red for oxidation) for reference. See Supplementary Discussion 12 for more detailed analysis.



**Extended Data Fig. 5 | Ionic conductivities and transference numbers of Li-Cu-CNF and Li-CNF.** **a**, Voltage profile of the galvanostatic Li plating and stripping between two ends of the Li-Cu-CNF with aligned cellulose fibres (length 1 cm) at 0.01 mA. **b**, EIS Nyquist plots of aligned Li-Cu-CNF materials of different lengths, ranging from 1 cm to 3 cm, for measuring the intrinsic conductivity of Li-Cu-CNF along the direction of the cellulose molecular chain. **c**, Resistance corresponding to the high-frequency semi-circle in **b** of the aligned Li-Cu-CNF with different lengths. **d**, EIS Nyquist plots of the aligned Li-Cu-CNF with a length of 3 cm and cross-sectional area of 0.03 cm<sup>2</sup> at different temperatures, ranging from 10 °C to 60 °C. **e, f**, EIS Nyquist plots of the Li-Cu-CNF paper electrolyte (through-plane) at different temperatures (**e**, 60 °C to 0 °C; **f**, -2 °C to -20 °C); **g**, the corresponding temperature-dependent through-plane ionic conductivity of the Li-Cu-CNF paper

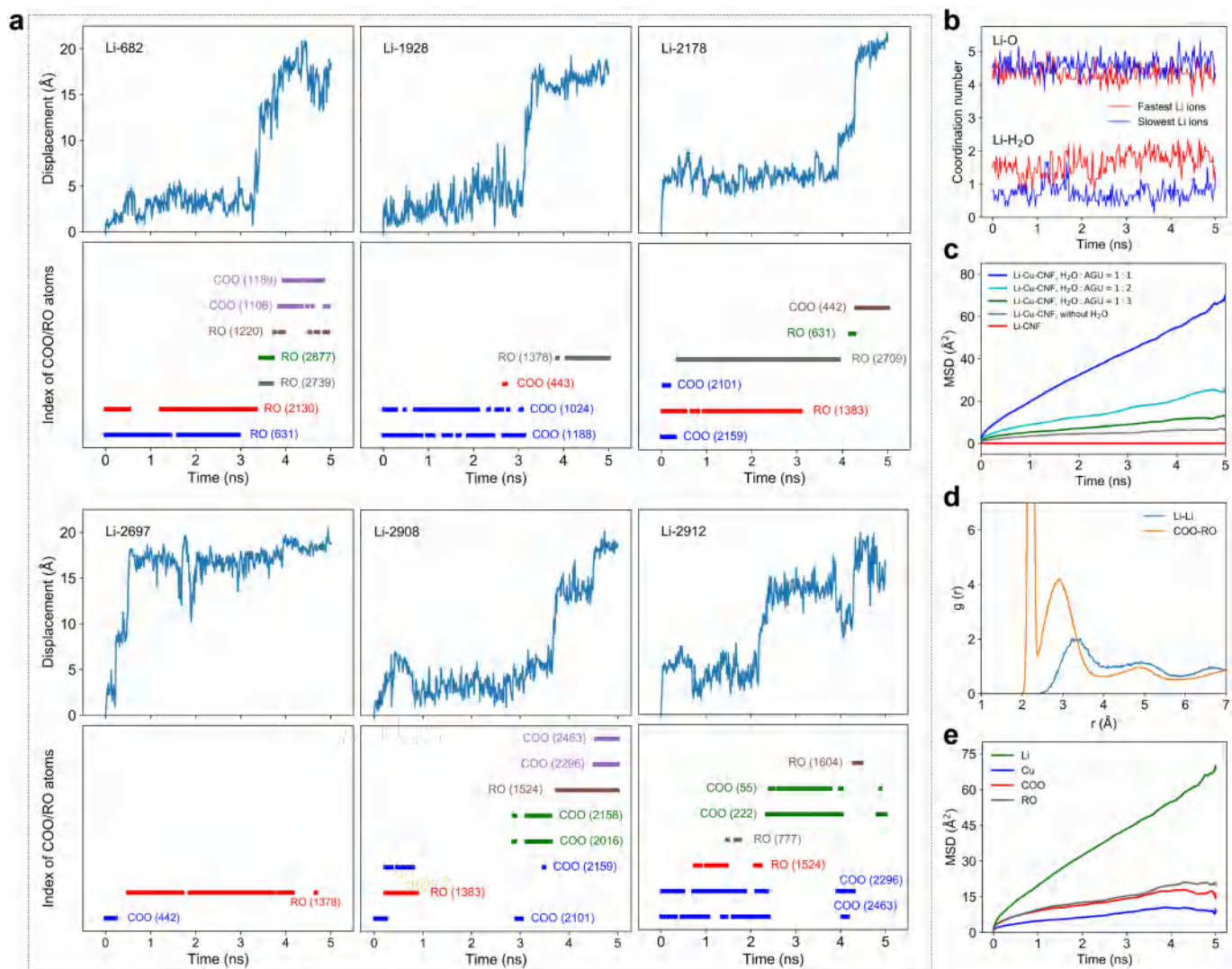
electrolyte. **h**, d.c. polarization curve of the Cu<sup>2+</sup> in the Li-Cu-CNF electrolyte in a Cu//Cu-CNF//Cu cell, showing that the Cu<sup>2+</sup> conductivity is  $1.0 \times 10^{-8}$  S cm<sup>-1</sup>, much lower than the Li<sup>+</sup> conductivity in Li-Cu-CNF. **i**, Simulated structure of Li-CNF by MD. The Li-CNF system consists of 16 cellulose chains surrounded by Li<sup>+</sup> and water molecules. Different chains are denoted by different colours. Li<sup>+</sup> ions are indicated by purple spheres and water molecules as stick models. The size of the Li-CNF system is given roughly. The simulations show that, without the participation of Cu<sup>2+</sup>, the Li<sup>+</sup> and water molecules adsorb only on the surface of the cellulose structures. **j**, d.c. polarization curve, and **k**, EIS Nyquist plots before and after polarization of the Li//Li-Cu-CNF//Li cell. **l**, d.c. polarization curve, and **m**, EIS Nyquist plots before and after polarization of the Li//Li-CNF//Li cell. **n**, Table showing the parameters measured by d.c. polarization and EIS for calculating the Li<sup>+</sup>-transference number.





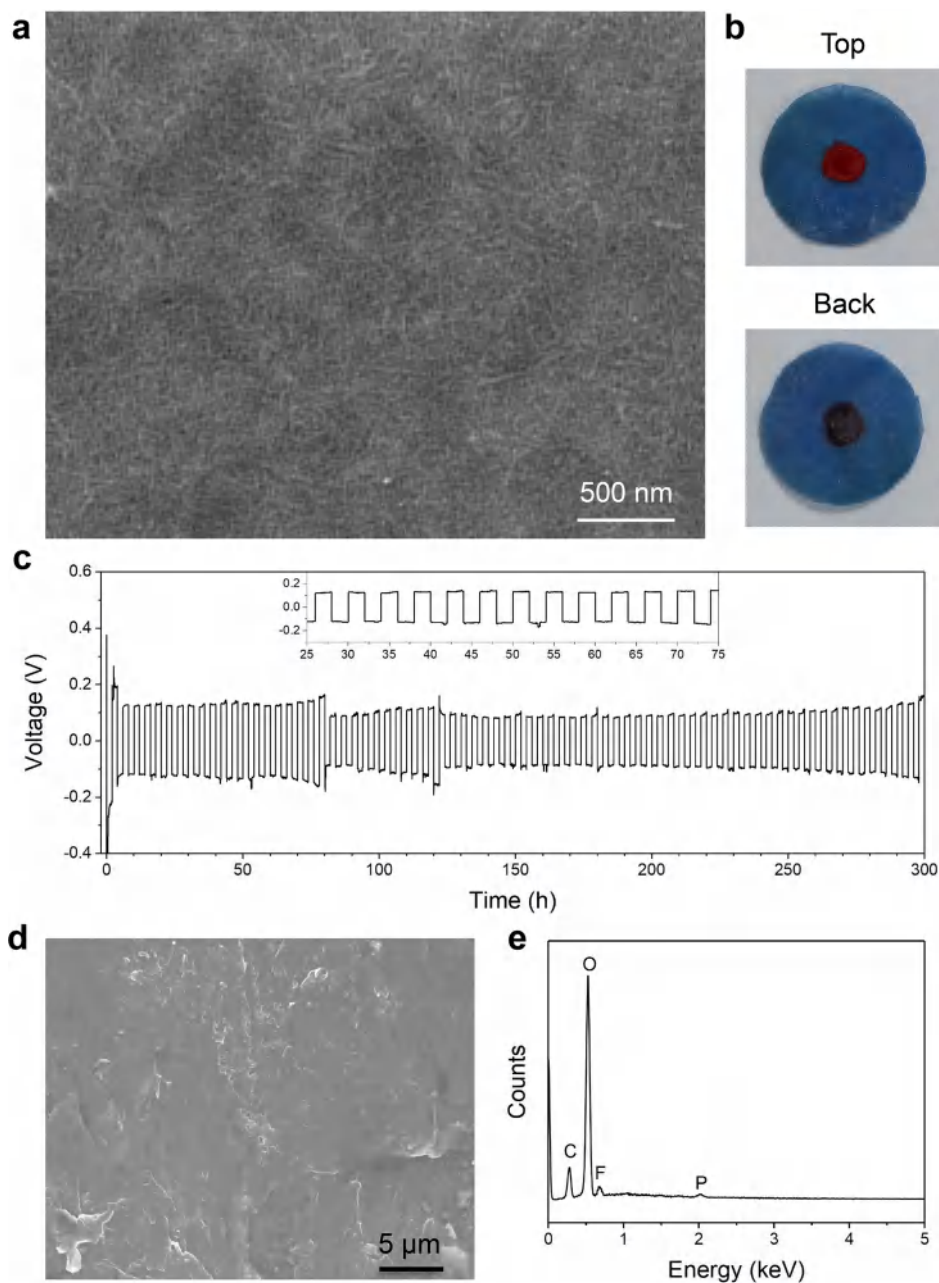
**Extended Data Fig. 6 | NMR analysis of Li-coordination environments and diffusion pathways.** **a**,  $^6\text{Li}$  NMR spectra and simulations for: **a**, Li-Cu-CNF; **b**, Li-CNF. **c**,  $^6\text{Li}$  NMR spectra for: **c**, CH $_2$ COOLi $\cdot$ 2H $_2$ O, and **d**, LiPF $_6$ , as references for the COO $\cdots$ Li and LiPF $_6$  peak assignments in Li-Cu-CNF. **e**,  $^6\text{Li}$  NMR spectra and simulations for: **e**, Li-Cu-CNF, and **f**, Li-CNF after  $^6\text{Li}$ - $^7\text{Li}$  tracer exchange, which was performed by cycling either the Li-Cu-CNF or the Li-CNF electrolyte (natural abundance: 92.4%  $^7\text{Li}$  and 7.6%  $^6\text{Li}$ ) between two  $^6\text{Li}$ -enriched metal electrodes (that is, symmetric  $^6\text{Li}$ /Li-Cu-CNF/ $^6\text{Li}$  cells). **g**, Table showing the amount of Li $^+$  in the different chemical environments of Li-Cu-CNF and Li-CNF before and after  $^6\text{Li}$ - $^7\text{Li}$  tracer exchange, derived from

the relative spectral areal integrals of the  $^6\text{Li}$  resonances in the NMR spectra shown in **a**, **b**, **e**, **f**. The normalized peak area for each sample (Li-Cu-CNF and Li-CNF, before and after  $^6\text{Li}$ - $^7\text{Li}$  tracer exchange) can be quantitatively compared between different samples as the normalized peak area is proportional to the amount of  $^6\text{Li}$  in each individual product. We took the total number of  $^6\text{Li}$  in the pristine Li-Cu-CNF (before  $^6\text{Li}$ - $^7\text{Li}$  tracer exchange) to be 100%, and calculated the 'relative  $^6\text{Li}$  number' of each component by comparing the fitted peak area (Extended Data Fig. 6a, b, e, f) with the total area of  $^6\text{Li}$  in the pristine Li-Cu-CNF (Extended Data Fig. 6a).



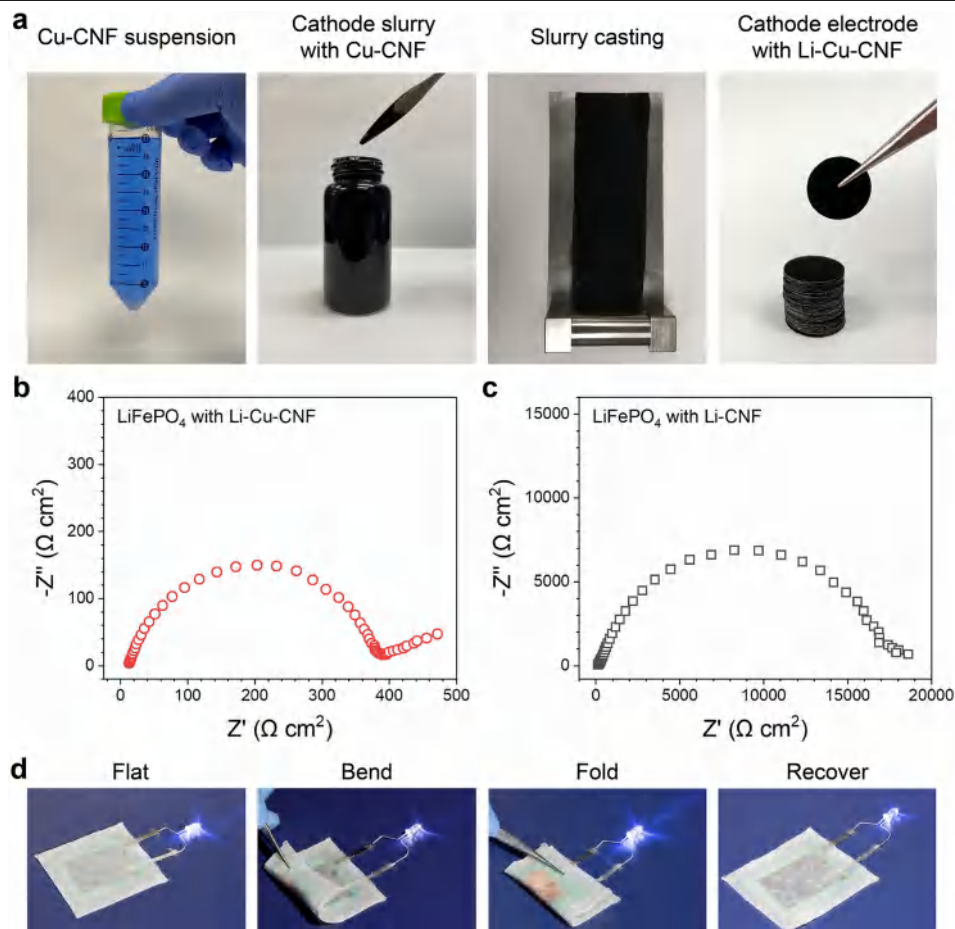
**Extended Data Fig. 7 | Numerical analyses of MD simulations for Li<sup>+</sup> transport in Li-Cu-CNF.** **a**, Displacement plots for six Li<sup>+</sup> ions that have displacements of more than 15.0 Å in the simulated Li-Cu-CNF system (Fig. 2i) with an H<sub>2</sub>O:AGU ratio of 1:1, and indexes of COO/RO atoms that are bonded to the six moving Li<sup>+</sup> ions (Li-O distance less than 2.5 Å). The different colours of the COO/RO atoms indicate they are from different cellulose chains. **b**, Coordination numbers of Li<sup>+</sup> ions coordinating with all available oxygen atoms (Li-O, including the oxygen atoms in cellulose and bound water molecules) and with just water molecules (Li-H<sub>2</sub>O) for the six fastest and six slowest Li<sup>+</sup> ions in the Li-Cu-CNF system with an H<sub>2</sub>O:AGU ratio of 1:1. **c**, MSD plots for Li-Cu-CNF systems with different number of water molecules, and for

the Li-Cu-CNF system with water molecules on the surface of the CNFs. **d**, Radial distribution functions (RDFs) for Li-Li and COO-RO pairs in Li-Cu-CNF with an H<sub>2</sub>O:AGU ratio of 1:1. The locations of the first peak of the Li-Li pair and the second peak of the COO-RO pair indicate the Li<sup>+</sup> hopping distance (roughly 3.0 Å) between the residence sites. The first peak of the COO-RO pair indicates the distance between the two O atoms within the same COO group. **e**, MSD plots for Li<sup>+</sup>, COO<sup>-</sup> and RO<sup>-</sup> groups and Cu<sup>2+</sup> in the simulated Li-Cu-CNF system with an H<sub>2</sub>O:AGU ratio of 1:1. The average MSD plots show that Li<sup>+</sup> moves fast while COO<sup>-</sup>, RO<sup>-</sup>, and Cu<sup>2+</sup> in the Li-Cu-CNF backbone move much more slowly. For further analysis, see Supplementary Discussion 13.



**Extended Data Fig. 8 | The Li-Cu-CNF paper electrolyte and its electrochemical performance.** **a**, Top-view SEM image of the Li-Cu-CNF paper electrolyte. **b**, Digital photos (top and back) of a permeability test of the Li-Cu-CNF paper electrolyte to demonstrate the denseness. **c**, Li plating/stripping cycling performance of the Li-Cu-CNF paper electrolyte at  $0.5 \text{ mA cm}^{-2}$ , with 2 h for each plating/stripping half cycle, for a total of 300 h at

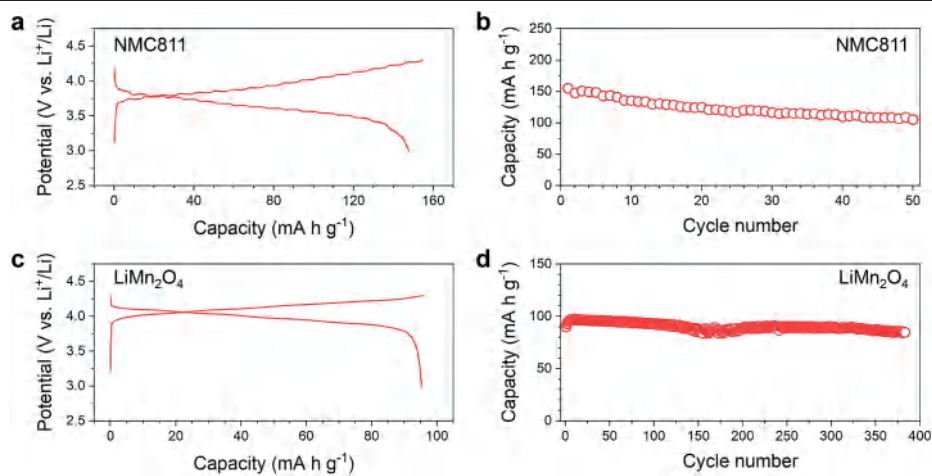
room temperature. **d**, SEM image and **e**, corresponding EDX spectrum of the Li-metal anode after long-term cycling with the Li-Cu-CNF paper electrolyte. The SEM image of the cycled Li anode shows a fairly smooth surface without Cu particles deposited on the surface. The EDX shows no detectable Cu element on the Li surface, and instead only C, O, F and P, indicating the formation of a solid electrolyte interphase (SEI) on the Li-metal anode.



**Extended Data Fig. 9 | Demonstration using Li-Cu-CNF as a paper electrolyte and ion-conducting binder for solid-state LiFePO<sub>4</sub> batteries.**  
**a**, Fabrication steps for incorporating the cathode material (LiFePO<sub>4</sub> here) with the Li-Cu-CNF ion-conducting binder via the traditional slurry-casting method. The Cu-CNF suspension is first mixed with the cathode material, CNT additive and sodium alginate binder in an aqueous solution to obtain the cathode slurry. The slurry is then cast on aluminium foil using a doctor blade and vacuum dried at 35 °C. The cathode electrodes are then soaked in Li<sup>+</sup>

electrolyte to achieve the insertion of Li<sup>+</sup> into the Cu-CNF, followed by vacuum drying to obtain solid electrodes containing the Li-Cu-CNF binder. **b, c**, EIS of the solid-state batteries using thick LiFePO<sub>4</sub> cathodes (roughly 120 μm), made by filtration-pressing with the addition of: **b**, Li-Cu-CNF; **c**, Li-CNF. **d**, A pouch solid-state battery made using a Li anode, the Li-Cu-CNF paper SPE, and a LiFePO<sub>4</sub> solid-state cathode containing the Li-Cu-CNF ion-conducting binder, which shows good flexibility while still powering an LED light.





**Extended Data Fig. 10 | Electrochemical performances of high-voltage cathodes with the solid-state Li-Cu-CNF electrolyte. a, b,** Typical galvanostatic charge/discharge voltage profile of a solid-state NMC811 cathode with the Li-Cu-CNF electrolyte cycled at 100 mA g<sup>-1</sup> and room

temperature (a); and its discharge capacities during cycling (b). **c, d,** Typical galvanostatic charge/discharge voltage profile of the solid-state LiMn<sub>2</sub>O<sub>4</sub> cathode with the Li-Cu-CNF electrolyte cycled at 50 mA g<sup>-1</sup> and room temperature (c); and its discharge capacities during cycling (d).